High Speed Switching and Rotational Dynamics in Small Magnetic Thin Film Devices*

Stephen E. Russek, Robert D. McMichael,
Michael J. Donahue, and Shehzaad Kaka

National Institute of Standards and Technology (NIST),
Magnetic Technology Division, 325 Broadway, Boulder, CO 80305, USA
russek@boulder.nist.gov

Abstract. The intent of this chapter is to review high-frequency magnetic device measurements and modeling work at NIST which is being conducted to support the development of high-speed read sensors, magnetic random access memory, and magnetoelectronic applications (such as isolators and microwaves components). The chapter will concentrate on magnetoresistive devices, those devices whose resistance is a function of the magnetic state of the device, which can in turn be controlled by a magnetic field. The low-frequency characteristics of magnetoresistive devices will be reviewed. Simulated high-frequency device dynamics, using single-domain and micromagnetic models, will be discussed. Next, high-speed measurements of magnetization rotation and switching in micrometer-size devices will be presented. The effects of thermal fluctuations and disorder on device dynamics will be examined, and high-frequency magnetic noise data will be presented. Finally, the need to understand and control high-frequency magnetic damping will be discussed, and a method for engineering high-frequency magnetization damping using rare-earth doping will be presented.

1 Introduction to High-Speed Magnetic Devices

Understanding and controlling magnetization dynamics in magnetic devices has become important as magnetic recording and magnetoelectronic technologies push toward operation in the gigahertz regime. Magnetization dynamics in magnetic thin films was intensively studied in the late 1950s when magnetic thin-film memories were proposed as a replacement for ferrite core memory [1,2,3]. It was recognized then that the intrinsic response times of magnetic thin films were in the nanosecond range. Such "millimicrosecond" response, which seemed very fast from the perspective of electronic technologies in 1958, is now a potential limitation of magnetic technologies, which must keep pace with semiconductor circuits that can operate well above 1 GHz. Concurrent with the requirement for faster device performance is

* Publication of NIST, not subject to copyright

B. Hillebrands, K. Ounadjela (Eds.): Spin Dynamics in Confined Magnetic Structures II,
Topics Appl. Phys. **87**, 93–156 (2003)

the need for reducing device dimensions well below 1 μm. These two requirements have initiated considerable interest in measuring, understanding, and controlling magnetization dynamics in small magnetic structures.

1.1 Background

A variety of magnetic devices have been developed in the last 50 years. During the 1970s, many sophisticated structures were developed for bubble memory and bubble logic based on perpendicular domains in yttrium iron garnet films [4,5]. These device structures included magnetoresistive sensors to read the bubble memory and magnetic circuits to propagate and control bubble motion. However, bubble memory was unable to compete with other memories, such as semiconductor and hard disk memory, and this magnetic device technology was not pursued. Magnetic devices came of age in the 1980s when devices based on anisotropic magnetoresistance (AMR) were proposed for read head sensors [7] and magnetic random access memory (MRAM) [8]. With the discovery and development of giant magnetoresistance (GMR) [9,10] and tunneling magnetoresistance (TMR) [11], the sophistication and utility of these magnetic device structures have advanced rapidly. The level of sophistication and atomic-scale control of material properties in magnetic devices now rivals that of Si and III–V semiconductor devices.

The intent of this chapter is to review high-frequency magnetic device measurements and modeling work at NIST, which is being conducted to support the development of high-speed read sensors, MRAM, and magnetoelectronic applications (such as isolators and microwaves components). The chapter will concentrate on magnetoresistive devices, those devices whose resistance is a function of the magnetic state of the device, which can in turn be controlled by a magnetic field. Section 1.2 will provide a brief introduction to magnetic device structures and will discuss their low-frequency response. Section 1.3 will review single-domain dynamic models of device response. These models treat each magnetic layer in the device as a single-domain, uniformly magnetized particle. Section 2 will discuss micromagnetic modeling, which allows spatial variation of magnetization and will review work at NIST on an object oriented micromagnetic modeling facility (OOMMF). Several examples of micromagnetic modeling of device dynamics will be presented, including magnetization reversal in a small rectangular magnetic element (μMAG standard problem 4) and a memory device based on a domain-wall trap. Section 3 will review methods of high-speed measurements of small magnetoresistive magnetic devices that can be made by incorporating the devices in high-bandwidth circuits. The output voltage is, in general, proportional to a component of the magnetization and, by monitoring the voltage, the time-dependent magnetization can be measured. Electrical measurement of magnetization dynamics has some advantages over other methods, such as high-speed magneto-optical measurement [6], in that it can be extended to

structures with dimensions well below 100 nm, can measure single-shot response (as opposed to averaged response), and it can measure dynamics in the complicated multilayer structures that are being used in high-speed magnetic technologies. Section 4 will review measurements of device rotation in response to field pulses transverse to the device's easy axis. This type of dynamic motion is quantitatively well described by simple dynamic models and provides a measurement of ferromagnetic resonance (FMR) and damping times in small magnetic structures. Section 5 will review measurements of magnetization reversal in devices that are designed for bistable applications such as MRAM. Understanding and controlling magnetization reversal in these small magnetic structures is one of the principal challenges in engineering MRAM circuits. In Sect. 6, we will describe the effects of disorder and thermal fluctuations on high-speed magnetization dynamics. Thermal fluctuations become increasingly important as the device size is scaled below 1 μm. These fluctuations lead to intrinsic magnetic noise that will be a fundamental limitation on device performance. One positive aspect of high-frequency magnetic noise is that it provides a powerful technique for studying the dynamics in magnetic nanostructures. Finally, Sect. 7 will discuss the control of magnetic damping.

1.2 Magnetic Devices

Practical magnetic devices require a combination of sensitivity to magnetic fields and an ability to control the magnetic state of the device precisely. Large magnetoresistance values have been observed in magnetic multilayers, such as Fe-Cr [9,12] and Co-Cu [13] multilayers, and in oxide materials such as La-Sr-Mn-O [14], but these materials, in general, have large saturation fields and a magnetic structure that is very difficult to control in small devices. For these reasons, the structures that are being developed for applications tend to be simple devices with two or three metallic magnetic layers. These devices, which include spin valves and magnetic tunnel junctions, share the same basic principle of operation: the resistance is a function of the relative orientation of adjacent magnetic layers. By applying a magnetic field, the relative orientation of the magnetizations can be changed, and the device can be used as a magnetic field sensor. Alternatively, the different resistance states can be used as data storage bits, which can be written by using an applied magnetic field produced by adjacent current-carrying lines.

In the simplest models of GMR [15] and spin-dependent tunneling [16], the change in resistance of a two-layer structure is proportional to the cosine of the angle θ between adjacent layer magnetizations: [1]

$$\frac{R - R_{||}}{R_{||}} = \frac{\Delta R}{2R_{||}}(1 - \boldsymbol{m_1} \cdot \boldsymbol{m_2}) = \frac{\Delta R}{2R_{||}}[1 - \cos(\theta)]\,, \tag{1}$$

[1] For recent reviews of electron transport calculations in GMR and TMR systems, see [17,18]

where R is the device resistance, $R_{||}$ is the resistance in the parallel state, ΔR is the difference in resistance between the parallel and antiparallel state, and $\boldsymbol{m_1}$ and $\boldsymbol{m_2}$ are the layer magnetization unit vectors. Deviations from this cosine dependence are predicted (in certain configurations) by more sophisticated GMR models [19]. The presence of anisotropic magnetoresistance will cause the measured magnetoresistance to deviate further from this simple angular dependence. However, for most devices, the cosine dependence is a reasonable approximation (see [20] and Fig. 1a), and the GMR signal can be interpreted as the spatial average of the projection of one layer's magnetization on the other. When one layer has a fixed magnetization direction, the GMR signal is then proportional to the average magnetization component of the free layer in the direction of the fixed layer.

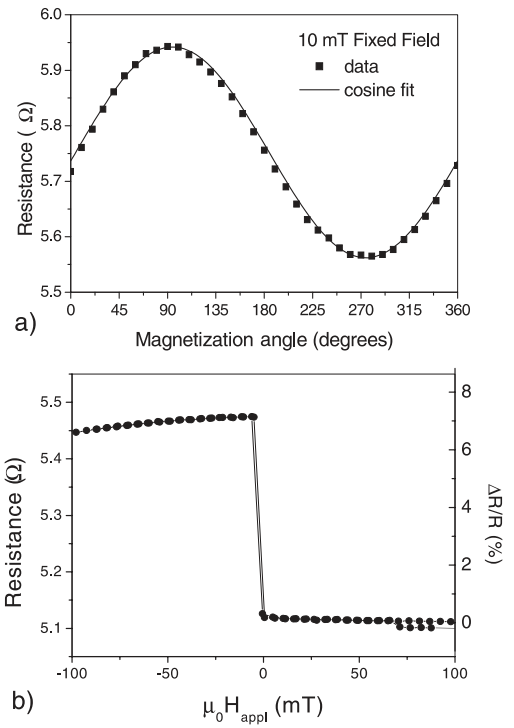

Fig. 1. (**a**) Magnetoresistive response of a SAF spin valve to a rotating magnetic field. The rotating magnetic field is large enough to align the free layer but too small to affect the fixed layer. The solid line shows a cosine fit to the data. (**b**) The magnetoresistive response of the same SAF spin valve due to a ramped magnetic field showing free layer switching and minimal response of the fixed layer to applied fields up to 100 mT. The layer structure is Ta(5 nm)/$Ni_{0.8}Fe_{0.2}$(5 nm)/Co(1 nm)/Cu(3 nm)/Co(2 nm)/$Ni_{0.8}Fe_{0.2}$(6 nm)/Ru(0.5 nm)/$Ni_{0.8}Fe_{0.2}$(4.3 nm)/FeMn(10 nm)/Ta(5 nm)

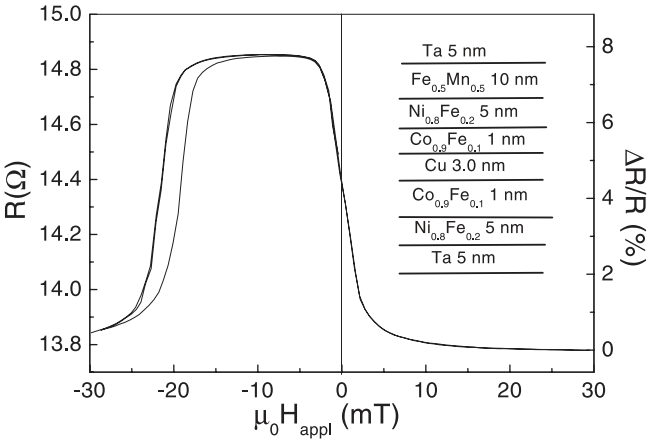

Fig. 2. Magnetoresistive response of a 4-μm wide spin valve in which the fixed layer is pinned perpendicularly to the free-layer easy axis. The field is applied perpendicularly to the free-layer easy axis. The free-layer magnetization rotates parallel and antiparallel to the fixed layer at low applied fields. In large negative applied fields, the fixed-layer switches into the applied field direction. The *inset* shows the layer structure

A spin valve is, conceptually, the simplest structure consisting of two decoupled magnetic layers [20]. One layer is pinned so that its magnetization direction is fixed, whereas the other is free to rotate in response to an applied magnetic field. The two layers must be in close electrical proximity so that nonequilibrium spin currents and polarization densities can be maintained. A typical top-pinned spin-valve layer structure is shown in the inset of Fig. 2.[2] Though the functional structure is conceptually simple, the physical structure is quite complex. An underlayer, typically Ta, is used to promote adhesion and the correct crystalline texture. A combination of magnetic alloys is used in the free layer to provide a soft magnetic response and high GMR. The spacer layer, typically Cu or a Cu alloy, is as thin as possible to maximize GMR yet allow the magnetic layers to be weakly coupled. The pinned or fixed layer can be made of a single magnetic layer or a trilayer that forms a synthetic antiferromagnet (SAF) [21]. A typical SAF structure is $Co_{0.9}Fe_{0.1}(2\,nm)/Ru(0.6\,nm)/Co_{0.9}Fe_{0.1}(1.5\,nm)$. The Ru layer provides a strong antiferromagnetic coupling that locks the surrounding CoFe magnetizations antiparallel to give a layer with a low net moment. A low net moment means that the SAF magnetization will be hard to rotate in an external field, as is the case with a natural antiferromagnet. The fixed layer is pinned by an

[2] In this chapter, we will quote magnetic field values in terms of the corresponding magnetic induction ($\mu_0 H$) in units of mT. This will allow easier comparison with field values reported elsewhere in this book in cgs units (1 mT corresponds to 10 Oe)

adjacent antiferromagnetic layer, such as $Fe_{0.5}Mn_{0.5}$, $Ir_{0.2}Mn_{0.8}$, $Pt_{0.5}Mn_{0.5}$, or $Ni_{0.5}Mn_{0.5}$ [22], so that the magnetization direction remains fixed up to large fields. The direction of the pin is set either by depositing the thin-film structure in a magnetic field or by subsequent annealing in a magnetic field. A capping layer, such as Ta, is used to protect the structures from corrosion and further processing.

A plot of the resistance of a spin valve, as a function of an applied hard-axis field, is shown in Fig. 2. In this device, the fixed layer is pinned perpendicularly to the free-layer easy axis. At zero field, the magnetizations are approximately perpendicular and, as the field is applied in the positive and negative directions, the free layer rotates parallel ($\theta = 0$) and antiparallel ($\theta = \pi$) to the fixed layer giving rise to a change in resistance ΔR. In large applied fields directed opposite to the pinning direction, the pinned-layer magnetization will also switch, and the system will return to a parallel low-resistance state. The cosine dependence of the resistance can been seen more explicitly in Fig. 1a in which the free-layer magnetization is rotated by a rotating applied field. This spin valve uses a SAF pinned layer to insure that the pinned layer remains fixed as the free layer rotates. There is little motion of the fixed layer in fields up to 100 mT, as can be seen in the magnetoresistance data shown in Fig. 1b.

In general, two device configurations are most useful in applications. For sensor applications, the fixed layer is pinned perpendicularly to the easy axis of the free layer. The field to be sensed is applied in the pinned direction (the same configuration as shown in Fig. 2). This configuration gives a linear response to small fields, as shown in Fig. 3a, which shows the resistance change for a 0.8-μm wide spin valve subject to small perpendicularly applied fields. Also shown is the calculated magnetization response using single-domain and micromagnetic models. The change in resistance is proportional to the average hard-axis magnetization of the free layer. The excellent fit to the micromagnetic model indicates that the resistance is a good parameter for describing the magnetization state of the device. For digital applications, such as MRAM, the fixed layer is pinned along the easy axis of the device [23]. Fields for switching the device are applied predominantly along the easy axis of the device, and a typical response curve is shown in Fig. 3b. The change in resistance is proportional to the average easy-axis magnetization of the free layer. The two stable states of the spin valve have different resistances that can be used to define a 0 or 1 state in digital memory applications.

The region of a GMR device that is sampled depends on the contact geometry. When the contact leads overlay the GMR element, the GMR signal from the covered ends is shorted by the leads, and only the region between the contact leads is sampled. If the contact leads abut, then the magnetic structure of the entire GMR device is sampled. Hence, GMR measurements can sample the average magnetization of the whole device or only a certain small region.

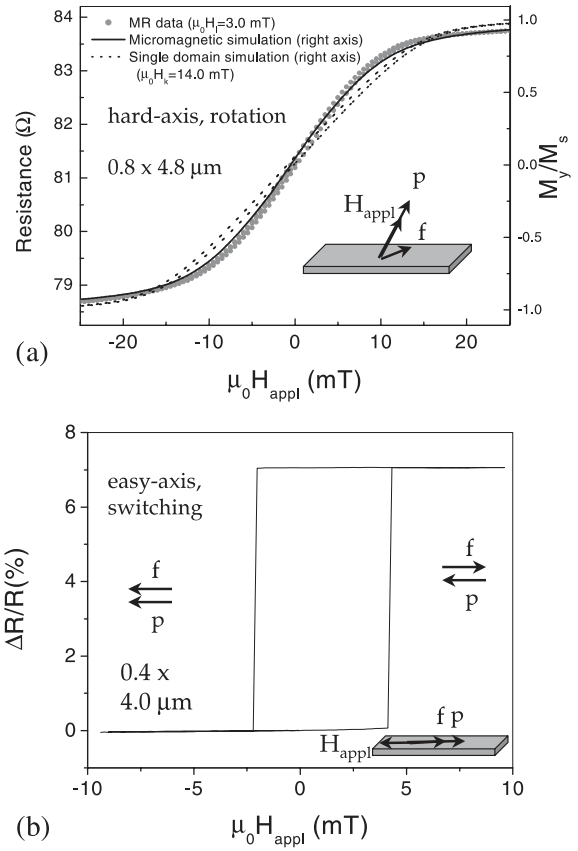

Fig. 3. (**a**) Magnetoresistive response of a spin valve in the sensor configuration in which the fixed layer is pinned perpendicularly to the free-layer easy axis and the field is applied along the hard axis. There is a constant 3-mT longitudinal bias field applied. Also shown is the calculated magnetization response from single-domain and micromagnetic (OOMMF) models. The model calculations use the measured device size and magnetization values and have no adjustable parameters. The single-domain model fit can be improved if the anisotropic field is allowed to vary. (**b**) Magnetoresistance of a 0.4-µm wide spin valve in the digital configuration in which the fixed layer is pinned along the free-layer easy axis and the field is also applied along the easy axis

There are many different permutations of the standard spin-valve structure, including bottom-pin spin valves with the fixed layer on the bottom and symmetrical spin valves with two pinned layers on top and bottom. A related structure, the pseudospin valve [24], is a simple sandwich consisting of two decoupled magnetic layers without any pinning (see Fig. 4). This structure uses differences in the layer properties, such as layer thickness, to promote relative magnetization motion between the two layers. For a device

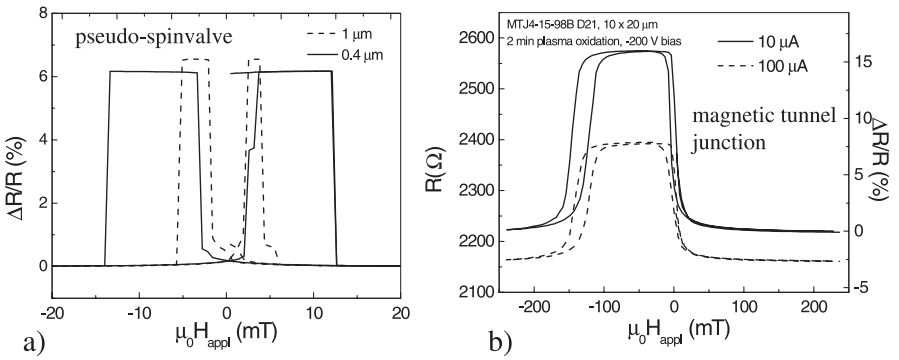

Fig. 4. (**a**) Magnetoresistive response of 0.4-μm and 1.0-μm wide pseudospin valves showing soft and hard layer switching. The layer structure is $Ni_{0.65}Fe_{0.15}Co_{0.2}$(6 nm)/$Co_{0.95}Fe_{0.05}$(1 nm)/Cu(3 nm)/$Co_{0.95}Fe_{0.05}$(1 nm)/$Ni_{0.65}Fe_{0.15}Co_{0.2}$(2 nm)/Ta(10 nm). (**b**) Magnetoresistive response of a 10-μm wide magnetic tunnel junction showing magnetic behavior similar to a spin valve. The response to two different bias currents is shown to illustrate the nonlinearity of TMR. The structure of the tunnel junction is $Ni_{0.8}Fe_{0.2}/Al_2O_3/Ni_{0.8}Fe_{0.2}/Fe_{0.5}Mn_{0.5}$

with different layer thicknesses, the thin layer has a smaller magnetostatic anisotropy field and is therefore the soft layer, whereas the thicker layer has a larger magnetostatic anisotropy field and is the hard layer.

Magnetic tunnel junctions consist of two layers separated by a thin insulator, typically 0.7 nm to 1.5 nm of Al_2O_3. The current is perpendicular to the plane of the film, and the device resistance depends on the relative orientations of the two magnetic electrodes. Magnetic tunneling devices are not linear, and the resistance and magnetoresistance vary with applied voltage and current, as seen in Fig. 4b. Though there are considerable differences in the nature of electrical transport, magnetic tunnel junctions are magnetically similar to spin valves. Magnetoresistive responses of up to 50% have been reported for magnetic tunnel junctions [25], which is considerably higher than the maximum of 19 and 25% reported for bottom-pin and symmetrical spin valve structures [26].

Most applications require that devices be sensitive to applied magnetic fields and therefore, require that the free layer rotate freely and not interact strongly with the fixed layer. This requires a separation layer greater than ~ 2 nm thick for a spin valve and ~ 0.7 nm for a tunnel junction. There are, however, always some interactions between the two layers. There is magnetostatic coupling between the layers due to surface roughness [27] which is sometimes referred to as "Néel" or "orange peel" coupling (refering to the dimpled texture of an orange). This coupling, in general, favors parallel alignment of the magnetizations and can be characterized by an effective coupling field created at one layer due to the other. This coupling field causes a loop shift or offset in the easy- and hard-axis magnetization and magnetoresis-

tance curves. This offset can be seen in Fig. 3b which shows an antiparallel-to-parallel switching field of −2.1 mT and a parallel-to-antiparallel switching field of 4.2 mT. In addition to "orange peel" coupling, there is magnetostatic coupling due to the free poles or charges (divergence of the magnetization) at the edges of each magnetic layer. To minimize energy, opposite magnetic charges like to be in close proximity, and therefore this interaction promotes antiparallel alignment of the magnetizations in adjacent layers. This coupling is sensitive to the geometry of the device and is more pronounced in devices with small aspect ratios [60].

In addition to the interaction with the applied field and the other magnetic layers, each layer also is influenced by the current-generated magnetic field. These fields are nonuniform within the device and are of substantial magnitude when the devices are driven with a large current to maximize the output signal.

All of these interactions must be included to model magnetic device response accurately, and they will be discussed more quantitatively in the next section.

1.3 Single-Domain Modeling

The simplest model of magnetic devices is to assume that the magnetization in each layer is uniform and can be described by a vector of constant magnitude, $\boldsymbol{M}_i$, denoting the i^{th} layer magnetization.[3] The evolution of the magnetization in response to applied fields can be described by a set of dynamic Landau–Lifshitz (LL) equations.[4]

$$\frac{\mathrm{d}\boldsymbol{M}_i}{\mathrm{d}t} = -\mu_0\gamma \boldsymbol{M}_i \times \boldsymbol{H}_{\text{eff}} - \frac{\mu_0\lambda_i}{M_{\text{s}}^2}\boldsymbol{M}_i \times (\boldsymbol{M}_i \times \boldsymbol{H}_{\text{eff},i})\,, \tag{2}$$

where γ is the gyromagnetic ratio[5], $H_{\text{eff},i}$ is the effective magnetic field, and λ_i is the LL damping parameter. The effective field, acting on the i^{th} layer, is the negative gradient of the free energy of the magnetic system with respect to the i^{th} magnetization. The effective field includes terms due to the external field, self-magnetostatic or demagnetizing fields, and magnetostatic and exchange interactions between the layers. The first term on the right describes precession about the effective field and conserves the energy of the system. The second term describes motion toward the effective field (or low-energy state) and describes damping or energy dissipation.

[3] We refer to this model as the single-domain model. It is also referred to as the Stoner, Stoner–Wohlfarth, or uniform rotation model, and is discussed in greater detail in the chapter by Fassbender

[4] For recent reviews of magnetization dynamics, see [33,34,35,36]

[5] Here, the gyromagnetic ratio is defined as a positive constant whose value is given by $\gamma = \frac{\mathrm{ge}}{2\mathrm{m_e}}$ where e and m_{e} are the electron change and mass respectively and $\mathrm{g} \approx 2$ for the material of interest in this article

The LL equation should be regarded as a phenomenological equation because many of the details of magnetization dynamics are not included in the LL model. This model (and related models) treats magnetic electrons as localized and independent from the conduction electrons though in reality the two systems interact and overlap. Further, the energy loss mechanisms (to phonons, conduction electrons, spin waves, and impurities) are not identified or explicitly included in the model. The damping parameter is treated as a constant when in fact there is theoretical and experimental evidence that the damping parameter can vary with the magnetization angle relative to the field direction and film normal, with the magnitude of the applied field, and with response frequency [32,37,38]. Several alternative dynamic equations have been proposed with different forms of the damping term. Notably, the Gilbert damping term, given by

$$\frac{\alpha}{M_\mathrm{s}}\boldsymbol{M}\times\frac{\mathrm{d}\boldsymbol{M}}{\mathrm{d}t}\,, \tag{3}$$

where α is the dimensionless Gilbert damping parameter, more accurately describes viscous damping in which damping is proportional to the magnetization velocity.

The Landau–Lifshitz–Gilbert (LLG) equation can be cast in the same form as the LL equation

$$\frac{\mathrm{d}\boldsymbol{M}_i}{\mathrm{d}t}=-\frac{\mu_0\gamma}{(1+\alpha^2)}\boldsymbol{M}_i\times\boldsymbol{H}_\mathrm{eff}-\frac{\mu_0\alpha\gamma}{M_\mathrm{s}(1+\alpha^2)}\boldsymbol{M}_i\times(\boldsymbol{M}_i\times\boldsymbol{H}_{\mathrm{eff},i})\,. \tag{4}$$

For small damping, the LL and LLG equations are identical with $\alpha=\lambda/\gamma M_\mathrm{s}$. For large damping (large λ), the LL equation predicts that the magnetic system will lose energy quickly and rapidly reach its low-energy state, whereas the LLG equation (for large α) predicts that the energy loss and approach to the low-energy state will become increasingly slow. The form of the phenomenological equation and its micromagnetic extensions, that best describes the magnetization response of magnetic devices, is still under debate and requires detailed understanding of the electronic structure, magnetic structure, and loss mechanisms in the particular magnetic system of interest. However, most magnetic devices have fairly low damping ($\alpha=0.01$–0.05), magnetization motions are predominantly in plane, and applied fields and anisotropic fields are in the range of 10 mT. Under these conditions, we do not need to distinguish between the LL and LLG equations, and we can, in most cases, model accurately by using the LL equations with a constant α.

In general, the energy of the magnetic system can contain many terms, including those due to external magnetic fields, magnetostatic energy, exchange energy, induced or crystalline anisotropic energy, spin currents, and strain. For most small magnetic devices, the energy is usually dominated by the external magnetic field, magnetostatic energy, and exchange interactions in adjacent layers with small separations (for example in the SAF).

The magnetostatic energy for a given layer can be separated into several components. The self-magnetostatic, or demagnetizing, energy is given by

$$E_{\mathrm{dm},i} = \frac{1}{2}\mu_0 \boldsymbol{M}_i \cdot \bar{\bar{\mathbf{N}}}_i \cdot \boldsymbol{M}_i \,, \tag{5}$$

where $\bar{\bar{\mathbf{N}}}_i$ is the self-demagnetizing tensor (whose trace = 1) of the i^{th} layer. Analytical expressions for the demagnetizing tensor can be found for simple shapes, including ellipsoids and rectangular parallelepipeds [28]. For all structures, except for perfect ellipsoids, the demagnetizing field varies across the device, and the calculated effective demagnetizing field, $H_{\mathrm{dm}} = -\bar{\bar{\mathbf{N}}}_i \cdot \boldsymbol{M}_i$, is the average of the demagnetizing field across the device volume. This nonuniform demagnetizing field gives rise to nonuniform magnetization that limits the accuracy of the single-domain models currently being discussed and necessitates using micromagnetic models described in Sect. 2. Demagnetizing fields are shape-dependent and can be quite large in small magnetic devices. For instance, for a rectangular Permalloy element ($\mathrm{Ni}_{0.8}\mathrm{Fe}_{0.2}$) with dimensions $l_x = 1.0\,\mu\mathrm{m}, l_y = 0.5\,\mu\mathrm{m}, l_z = 0.005\,\mu\mathrm{m}$, the demagnetizing factors are $N_x = 0.009, N_y = 0.018, N_z = 0.973$, leading to an in-plane anisotropy field of $\mu_0 H_{\mathrm{k}} = \mu_0(N_y - N_x)M_{\mathrm{s}} = 9.3\,\mathrm{mT}$.[6]

The magnetostatic interaction between layers in the single-domain model can be approximated by two components. The magnetostatic fields, generated by the divergence of the magnetization (effective magnetic charges) at the edges of the device, lead to an interaction term [29]

$$E_{\mathrm{dm},ij} = \frac{1}{2}\mu_0 \boldsymbol{M}_i \cdot \bar{\bar{\mathbf{N}}}_{ij} \cdot \boldsymbol{M}_j \,, \tag{6}$$

where $\bar{\bar{\mathbf{N}}}_{ij}$ is the mutual demagnetizing tensor (whose trace is 0) between the i^{th} and j^{th} element. This interaction favors antiparallel alignment, as discussed in the previous section, and is again very dependent on the shape of the device. This interaction is of the same size as H_{k}. A second term, that describes magnetostatic coupling due to effective charges generated by the roughness of the magnetic layer (orange-peel coupling), can be approximated by

$$E_{\mathrm{co},ij} = -E_{\mathrm{co}} \boldsymbol{m}_i \cdot \boldsymbol{m}_j \,, \tag{7}$$

where E_{co} is the phenomenological coupling energy and $\mu_0 H_{\mathrm{co},i} = E_{\mathrm{co}}/M_{\mathrm{s},i}$ is the phenomenological coupling field. The coupling field can be related to the interfacial roughness and is proportional to the layer magnetizations. In

[6] In this article, we use the convention that the x direction is the easy axis of the device, the y direction is the in-plane hard axis, and the z direction is the direction perpendicular to the film plane. For the devices described here, magnetostatic shape anisotropy usually dominates, and the easy axis is along the long axis of the device. Hence, the in-plane easy and hard axes are referred to as the longitudinal and transverse directions, respectively

general, the coupling field is positive and favors parallel alignment of the magnetizations. For the devices discussed here, typically, $\mu_0 H_{\rm co} = 0.5$–$2\,{\rm mT}$.

Similarly, the exchange interactions between magnetic layers, which are separated by thin spacer layers such as in the SAF structure, need to be included and are characterized by phenomenological interlayer exchange coupling J:

$$E_{{\rm ex},ij} = -J_{ij}\boldsymbol{m}_i \cdot \boldsymbol{m}_j \,. \tag{8}$$

The exchange fields, $\mu_0 H_{{\rm ex},i} = J_{ij}/M_{{\rm s},i}$ can be quite large, of the order of 0.1 T to 1 T, and for typical device operation, for which the applied fields are of the order of 5 to 10 mT, the exchange fields, it can usually be assumed, rigidly couple adjacent layers. Exchange bias, which refers to the interaction between an antiferromagnetic and a ferromagnetic layer, can also be modeled as a interaction field whose direction is set during deposition or subsequent magnetic annealing. Exchange bias also requires a uniaxial anisotropic term (one in which the energy is proportional to the square of the cosine of the relative angle between the layers) to model observed device behavior accurately [30].

The current-induced fields, which may at first seem to be one of the simplest interactions, are quite complicated to calculate. The current profile cannot be calculated from bulk conductivity values because most of the layers are of the order of, or smaller than, the electron mean free path and interfacial scattering strongly modifies the current distribution. The current-induced fields can be quite large for devices used in applications, such as read head sensors, in which the current is maximized to produce the largest voltage signal. The fields are typically of the order of $5\,{\rm mA/\,\mu m} = 5\,{\rm kA/\,m}$ (which corresponds to 6 mT). It is important to note that current-induced magnetic fields cannot be modeled as uniform external fields and can give rise to dynamic responses that cannot be excited by external fields.

The final type of interaction that needs to be included (for the devices covered in this chapter) is a random thermal field [31]. This field has an average magnitude that is proportional to $k_{\rm B}T$ and is inversely proportional the volume of the magnetic element. The effects of thermal fluctuations are usually not important except when the device size becomes smaller than approximately 1 μm or when switching magnetization near the critical switching threshold. Thermal fluctuations will be discussed in detail in Sect. 7. However, it is convenient to include a thermal term in all single-domain, dynamic simulations, so that the system does not get stuck in unstable equilibrium positions.

If the applied fields vary slowly, the dynamic response can be described adequately by just the damping term. In this limit, the quasi-static or adiabatic limit, the device magnetization follows a trajectory of minimum energy. Equivalently, the magnetization is always aligned in the effective field direction. The criterion for being in the quasi-static limit is that the applied field changes slowly on a timescale given by the energy relaxation time (for

$\alpha << 1$) $\frac{1}{\tau_E} = \gamma\mu_0\alpha[(H_l + M_s) + (H_l + H_k)]$ where H_l is the bias field along the easy axis [32,38]. The quantity in the brackets is just the sum of the in-plane and out-of-plane stiffness fields perpendicular to the easy axis. For the materials of interest, the energy relaxation time is of the order of 1 ns. Figure 5a shows a series of energy diagrams of a single-domain magnetic layer for several values of an applied perpendicular field.[7] The dots indicate the minimum-energy trajectory that corresponds to the standard *Stoner–Wohlfarth* rotational model [39]. Figure 5b shows the simulated single-domain response of a thin-film device, calculated using the LL equation, to a quasi-static hard-axis field. It is important to remember that dynamic models must be able to calculate accurately the low-frequency quasi-static device response as well as the high-frequency response.

In the limit of slowly applied fields, no energy is dissipated in the magnetic system if the system stays within one potential well. Energy is transferred from the external field into magnetostatic energy and then back into the applied magnetic field. Figure 3a shows a comparison of the measured and single-domain model response of a spin valve for quasi-static hard-axis fields. Note that, using the measured device dimensions and the bulk values for the magnetization, the single-domain model predicts a response stiffer than the measured data. However, the single-domain simulation is reasonably good if

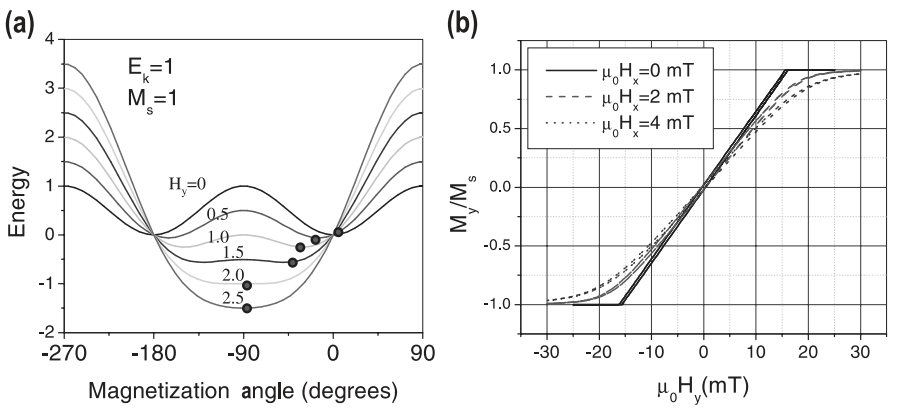

Fig. 5. (**a**) In-plane magnetostatic energy surface as a function of the in-plane magnetization angle for a single-domain, thin-film element with different values of applied hard-axis fields. The dots indicate the quasi-static trajectory (**b**) Quasi-static hard axis response calculated with the LL equation for a single-domain, thin-film element (the y direction is along the in-plane hard axis) for several values of easy-axis bias fields

[7] Figure 5a shows the sum of the in-plane magnetostatic energy and the Zeeman energy. The total energy is the sum of this energy with the out-of-plane magnetostatic energy. The out-of plane magnetostatic energy plays a role very similar to the kinetic energy of a particle moving in a potential well

the anisotropic field is allowed to vary to fit the data. Micromagnetic models, described in the next section, accurately calculate the magnetostatic fields and there is no need to introduce an effective magnetostatic anisotropic field.

If the applied field has a rise time shorter than the energy relaxation time, then the precessional term can drive the magnetization across a large range of motion before energy is dissipated. This type of motion corresponds to a trajectory that oscillates many times around energy minima before finally settling into a low-energy state. This regime is often referred to as the "precessional" or "dynamic" regime. An example of this type of motion in Fig. 6 shows the simulated response of a 0.5 μm × 1 μm single-layer device to a 200-ps transverse field pulse. The applied field turns off before the magnetic system can attain equilibrium. The device relaxes through damped precessional motion. Note that there is a small component of magnetization perpendicular to the plane of the film. Although the motion remains predominantly in the plane of the film, the small perpendicular component generates large demagnetizing fields due to the large demagnetizing factor in the perpendicular direction and contributes to driving the precessional motion. The magnetostatic energy of the system oscillates between the perpendicular and transverse components, as the system relaxes.

Larger easy-axis applied field pulses can cause a magnetic device to switch between energy minima (stable easy-axis states). An example of such a switch

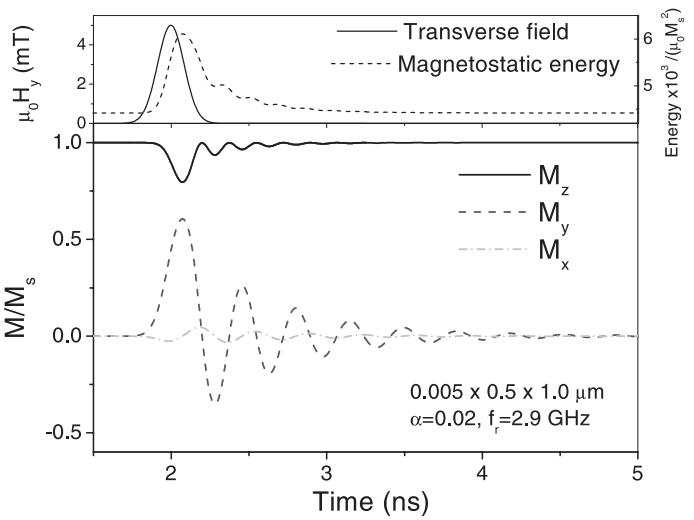

Fig. 6. Single-domain LL simulation of a spin valve subjected to a 200-ps transverse field pulse. The damping constant is $\alpha = 0.02$, and the resonance frequency is $f_r = 2.9$ GHz. Here, x, y, and z refer to the longitudinal, transverse, and perpendicular directions, respectively. The top panel shows the applied field pulse and the relaxation of the magnetostatic energy (the total energy minus the energy from the applied field). The energy relaxation time is approximately 0.7 ns

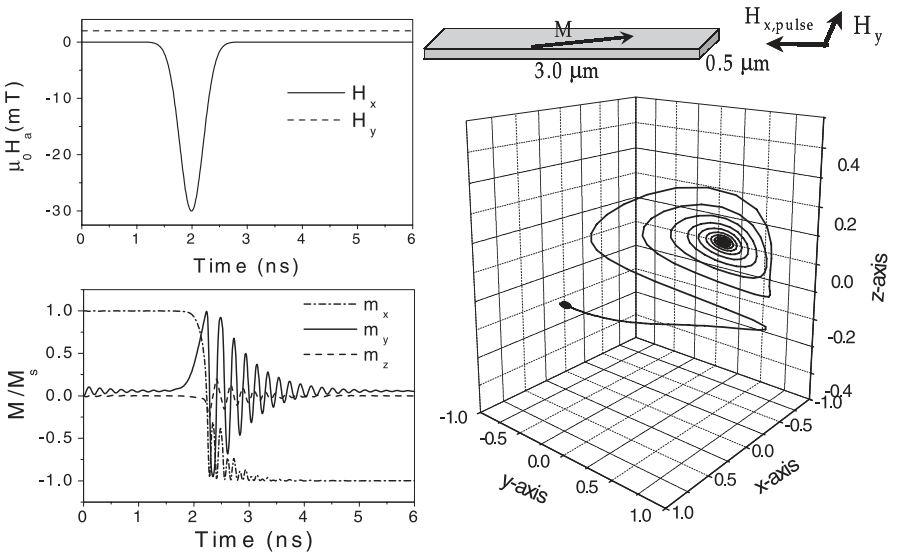

Fig. 7. Single-domain LL simulation of a 3.0 μm × 0.5 μm spin valve subjected to a 30-mT, 200-ps longitudinal field pulse. The device switches by precessing around a combination of the demagnetizing and applied fields. A 2.5-mT transverse bias field is applied, the damping constant is $\alpha = 0.01$

is shown in Fig. 7 in which a 0.5 μm × 3.0 μm single-layer device is driven by a 200-ps pulse directed opposite to the initial magnetization direction. Note that the initial response is precession about the perpendicular demagnetizing field followed by a damped precessional relaxation to the new easy-axis position. Modeling of high-speed switching of a single-domain particle is described in much greater detail in the chapter by *Fassbender*.

The examples given above include dynamics in only a single layer, whereas most devices have two or more magnetic layers. In a spin valve with a modest to strong pin, it is a reasonable approximation to ignore the dynamics in the fixed layer. Figure 8 shows the results of two-layer, single-domain calculations in which both the free and the pinned layer undergo dynamic motion. The simulation is done for a 0.5 μm × 1.0 μm spin valve with the fixed layer pinned by a 25-mT field perpendicular to the easy axis. Figure 8a shows the quasi-static response, which is qualitatively similar to the measured data presented in Fig. 2. The magnetostatic interaction between the layers, due to the edge charges, causes the free layer in the zero-field state to rotate off the easy axes toward the direction antiparallel to the fixed layer. This is seen as a shift in the spin valve response (which is proportional to the cosine of the relative angle between the free- and fixed-layer magnetizations) toward the antiparallel state. Figure 8b shows the device response to a 200-ps transverse field pulse similar to that shown in Fig. 6. The fixed layer undergoes small-angle oscillations ($< 5°$) with higher frequency components. However, the fixed-layer

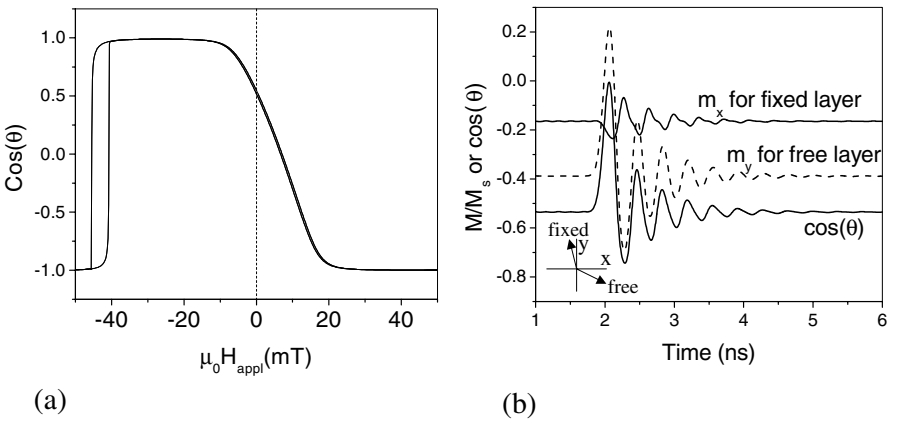

Fig. 8. Single-domain LL simulations of a 0.5 μm × 1.0 μm spin valve in which both the free and fixed layer are allowed to undergo dynamic motion. The fixed layer has a pinning field of 25 mT, and both layers have a damping constant of $\alpha = 0.02$. (**a**) Simulated quasi-static response of the spinvalve. (**b**) Dynamic response of the spin valve subjected to a 200-ps Gaussian transverse field pulse. Note that, due to the magnetostatic interactions, the quiescent position of the free layer has rotated 31° off its easy-axis position to an orientation more antiparallel to the fixed layer. The fixed layer undergoes only a small angle response, and the device response (proportional to the cosine of the angle between the magnetizations) is due predominantly to the free-layer motion

motion has little effect on the device output, as seen by comparing Fig. 8b to the transverse magnetization plotted in Fig. 6.

For pseudospin valves, in contrast to spin valves, it is important to consider the simultaneous magnetization dynamics in both layers. Figure 9 shows the simulated quasi-static and dynamic response of a 0.5 μm × 1 μm pseudospin valve. Two modes of the magnetization response can be identified: a high-frequency oscillation of the two magnetizations precessing together and a low-frequency oscillation of the magnetizations precessing in opposition. Due to the cancellation of magnetic charges when the moments are precessing in opposition, this motion has a smaller magnetostatic energy and is therefore softer. This type of soft mode, in which the magnetostatic energy is minimized, can play an important role is reversing a multilayer device by using small applied fields. The GMR response measures only the low-frequency mode in which there is relative motion between the layers, as in the lower plot of Fig. 9b. It is important to remember that the GMR signal measures only modes in which there is relative motion between the layers and those that have a nonzero spatial average across the sampling volume.

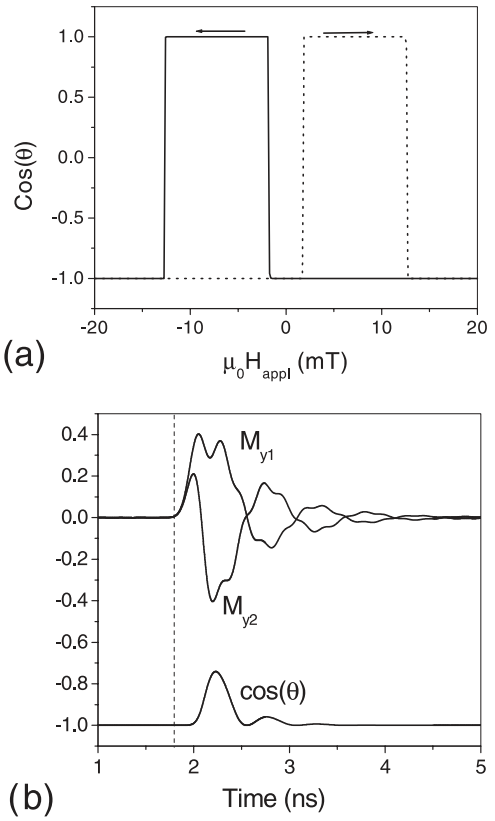

Fig. 9. Simulated single-domain LL response of a 0.4 μm × 3.0 μm pseudospin valve with soft and hard layers of 4 nm and 6 nm thick, respectively. Both layers have a damping constant of $\alpha = 0.02$. (**a**) Simulated quasi-static response of a pseudospin valve; (**b**) dynamic response of the same pseudospin valve to a 200-ps transverse Gaussian field pulse. In the initial state, the magnetizations are parallel. The initial response to the field pulse is that the magnetizations rotate together. This motion rapidly converts to the lower frequency mode in which the magnetizations rotate in opposite directions

2 Micromagnetic Simulations of High-Speed Device Dynamics

To accommodate nonuniform applied fields, nonuniform magnetostatic fields, and nonuniform magnetization configurations that can occur in devices, a micromagnetic approach is needed. Each region of interest is discretized, i.e., conceptually cut into a number of small subregions, or cells (usually of the order of 1–10 nm on a side). The behavior of the magnetization is then calculated based on the response of the magnetization in each cell to the local field consisting of the applied field, exchange interactions with the magnetization

in neighboring cells, local anisotropy, and dipolar interactions. Micromagnetic calculations are discussed in more detail in the chapter by *Schrefl* et al. and in [36].

For calculations of quasi-static behavior, it is often sufficient to calculate the lowest energy configuration of the magnetization in a given applied field. However, for high-speed applications, the dynamics must be calculated, typically, by using the Landau–Lifshitz or Landau–Lifshitz–Gilbert equations of motion, (2 and 4). These micromagnetic models can calculate the high-frequency nonuniform magnetization response due to realistic device shapes, magnetic disorder (arising from nonuniform magnetic properties), and nonuniform applied field pulses. These micromagnetic models still rely on phenomenological dynamic equations and have the limitations of these models. There is an important distinction between the damping terms included in micromagnetic models compared to those in single-domain models. The energy loss term in single-domain simulations includes losses to spin waves as well as energy that is transferred out of the magnetic system. The micromagnetic calculation inherently includes energy transfer to spin-wave modes, and the damping term includes only energy loss mechanisms that transfer energy out of the magnetic system.

In this section, we describe work by the micromagnetic modeling activity group (μMAG), which was formed at NIST in 1995 to address fundamental issues in micromagnetic modeling. The primary goals of μMAG are to

- foster communications between micromagnetic modelers
- develop standard problems and post submitted solutions
- develop portable, extensible public domain programs and tools for micromagnetics.

We present solutions to standard problem No. 4 to demonstrate some of the issues involved in the micromagnetic calculations of magnetization reversal in small magnetic elements. Next, we discuss micromagnetic calculations of rotation and switching in magnetic devices nominally designed to operate as single-domain structures. Finally, we will discuss the micromagnetics of domain walls and devices that incorporate domain walls.

2.1 NIST Object Oriented MicroMagnetic Framework (OOMMF)

The software portion of the μMAG initiative is OOMMF, a public domain micromagnetics package developed at NIST by Michael Donahue and Donald Porter. It is written using a combination of C++ and Tcl/Tk that makes the package both extensible and portable. Contributed modules may be activeted in the code by simply placing them in a distinguished directory and recompiling – no modification of the distributed source code is necessary. OOMMF runs on Windows and most Unix systems. Sourcecode and Windows executables are available for downloading at `http://math.nist.gov/oommf/`.

The first release in January 1998 supported a two-dimensional array of square cells with 3 d spins, allowing simulation of single-layer thin films. This code was used to provide submissions to μMAG standard problems Nos. 1, 2, and 4 [40,41,42]. Development versions of a fully 3 d solver, allowing a 3 d array of rectangular cells, were released, starting in November 2000. In this solver, all material constants may be specified on a point-by-point basis, so multilayer devices with arbitrary geometries can be modeled. The input problem specification file provides support for embedded Tcl scripts, allowing considerable run-time control and flexibility. For efficiency, the self-magnetostatic field is calculated using a fast Fourier transform accelerated convolution. Dynamic magnetization evolution is modeled using the Landau–Lifshitz–Gilbert differential equation (4), but direct energy minimization modules are available for quasi-static problems. Other features include long-range bilinear and biquadratic RKKY-style surface exchange energies and time-varying applied fields. Both interactive and batch execution modes are supported. Additional details on the OOMMF micromagnetic package are available in [41,43,44].

2.2 Standard Micromagnetic Problems

The μMAG standard problems are intended to provide benchmarks to test methods and software for micromagnetic calculations. To make the tests as relevant as possible, we try to make material parameters and geometries typical for device designs. The standard problems specify material parameters and geometry, applied fields, and the quantities to be calculated. The standard problem definitions and their submitted solutions are posted at `http://www.ctcms.nist.gov/~rdm/mumag.html`.

Standard problem No. 4 is designed to test the ability to calculate magnetization dynamics in a 500 nm × 125 nm × 3 nm slab of magnetic material with the following material parameter specifications: exchange stiffness $A = 1.3 \times 10^{-11}$ J/ m, magnetization $M_s = 8.0 \times 10^5$ A/ m, anisotropy $K = 0$ J/ m^3, and damping $\alpha = 0.02$. This problem illustrates many of the details and complexities of magnetization reversal in devices such as MRAM elements. The first step is to calculate an equilibrium "S-state" such as that

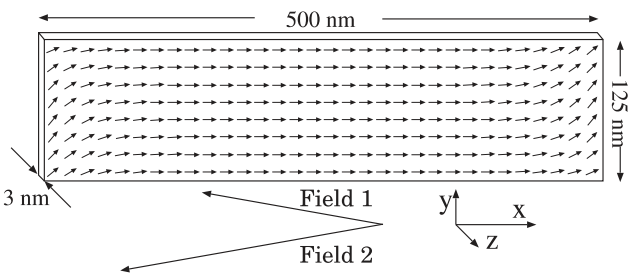

Fig. 10. Geometry of standard problem No. 4 with initial S-state

shown in Fig. 10.[8] Then, either of two switching fields is instantaneously applied, and magnetization is calculated as a function of time as it switches and comes to equilibrium in the applied field. The desired outputs are the vector components of spatially averaged magnetization as a function of time. The two switching fields are defined as

- *Field 1*: $\mu_0 H_x = -24.6\,\mathrm{mT}$, $\mu_0 H_y = 4.3\,\mathrm{mT}$, $\mu_0 H_z = 0.0\,\mathrm{mT}$, which is a field of approximately 25 mT, directed 170° counterclockwise from the positive x axis, and
- *Field 2*: $\mu_0 H_x = -35.5\,\mathrm{mT}$, $\mu_0 H_y = -6.3\,\mathrm{mT}$, $\mu_0 H_z = 0.0\,\mathrm{mT}$, which is a field of approximately 36 mT, directed 190° counterclockwise from the positive x axis.

Both of these fields have approximately 1.5 times the quasi-static coercivity of fields applied in the directions of Field 1 and Field 2. The most important difference between the two switching fields is in their direction relative to the magnetization in the initial S-state. Field 1 exerts a torque on the magnetization in the initial state that is counterclockwise everywhere. Field 2 exerts a counterclockwise torque near the ends of the rectangle and a clockwise torque in the central region of the rectangle.

Solutions have been submitted by five groups:

- G. Albuquerque, J. Miltat, and A. Thiaville, Lab. Physique de Solides, Univ. Paris-Sud and CNRS, Orsay, France.
- R. D. McMichael, M. J. Donahue, and D. G. Porter, NIST, Gaithersburg, MD, USA, and J. Eicke, George Washington University, Washington, DC, USA.
- L. Buda, L. Prejbeanu, U. Ebels, and K. Ounadjela, Institut de Physique et Chimie des Matériaux, Strasbourg, France,
- E. Martinez, L. Torres, and L. Lopez-Diaz, Departamento de Fisica Aplicada, Universidad de Salamanca, Salamanca, Spain.
- José L. Martins and Tania Rocha, INESC, Lisbon, Portugal.

For purposes of comparison, we find that the spatial average of the y component of magnetization $\langle M_y \rangle$ best displays differences among the results submitted. The plots are shown in Figs. 11 and 12. For both Field 1 and Field 2, the x component of magnetization $\langle M_x \rangle$ passes through zero about 0.14 ns after the field is applied, and there is not a large difference in the characteristic time required for the magnetization to ring down after the switching is more or less complete. However, the switching mechanism is very different for the two applied fields.

As Field 1 is applied, the magnetization everywhere in the sample experiences a torque that rotates the magnetization counterclockwise. Though

[8] A rectangular element has two equilibrium magnetization states, an "S" state in which the end spins are canted in the same direction and a "C" state in which the end spins are canted in opposite directions [36]

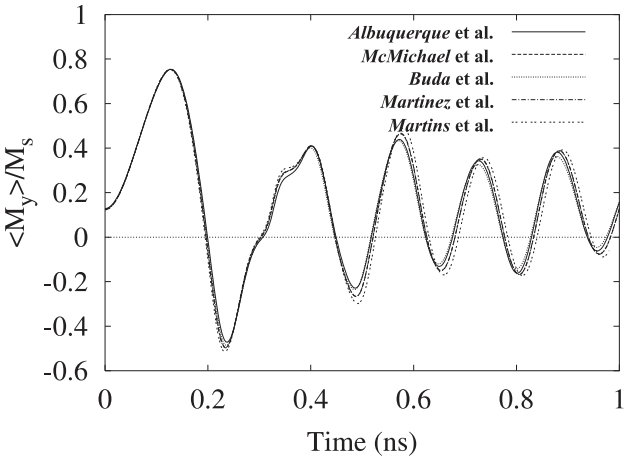

Fig. 11. Spatial average of M_y in standard problem No. 4 after Field 1 is applied. M_x crosses zero at about 0.14 ns

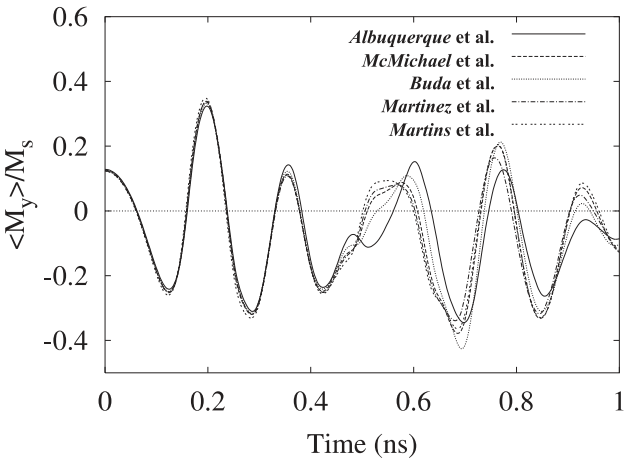

Fig. 12. Spatial average of M_y in standard problem No. 4 after Field 2 is applied. M_x crosses zero at about 0.14 ns

a counterclockwise rotation of the magnetization may be intuitive, the LLG equations of motion, (4), dictate that the magnetization precesses around the effective field. In the equilibrium state, the torque on the magnetization is zero. In the instant after Field 1 (H_1)is applied, the torque vector, $\mu_0 \mathbf{M} \times H_1$, initially points in the $+z$ direction, and the magnetization rotates toward the $-z$ direction. As the magnetization grows in the $-z$ direction, a magnetostatic field develops in the $+z$ direction, and this magnetostatic field rotates the magnetization in the x–y plane.

The torque applied by Field 1 is greatest near the ends of the sample where there is a significant y component of magnetization in the initial state. As a result, the magnetization near the ends rotates faster than the magnetization in the large central region of the sample, and partial domain walls form that propagate inward from the ends of the sample. The annihilation of these partial walls in the center of the sample is accompanied by some large amplitude oscillations of the magnetization that eventually damp out.

As Field 2 is applied, the magnetization rotates counterclockwise near the ends, as described above, but the sign of the torque is opposite in the center, so the magnetization in the center initially rotates clockwise. Given the oppositely directed rotation in the middle and at the ends, extrapolation forward in time would indicate a final state where the magnetization is nearly aligned with Field 2, except for two 360° walls. This is very nearly what happens in the full calculation, except that as the magnetization oscillates, the 360° walls move to the ends of the sample and disappear. In this last step, starting at about 0.45 ns, there are large exchange torques, where the magnetization varies rapidly among a few cells. As shown in Fig. 12, the solutions submitted begin to diverge from one another at this time.

At this time, the reasons for the divergence of the solutions are not known, but speculation includes questions about the adequacy of the discretization in both space and time. Rapid spatial variations in magnetization require fine discretization, and the accompanying large exchange torques require fine discretization in time to resolve the rapidly varying magnetization. Efforts to resolve differences between solutions by decreasing the time step and the discretization size have not been entirely successful. It may also be possible that highly excited magnetization goes into chaotic motion, so that it becomes sensitive to initial conditions and noise such as roundoff errors or differences between compilers and processors.

The work on standard micromagnetic problems illustrates that care must be taken when using micromagnetic models to calculate the high-speed dynamics of magnetic devices. For complex magnetization motions, subtle differences in the way the calculations are carried out may yield different results.

2.3 Modeling of Magnetic Rotation and Switching

In many magnetic device applications, it is hoped that the device magnetization will resemble that of a single-domain particle and will respond to applied fields in a uniform manner. We can distinguish between two types of magnetization motion: rotation and switching. Rotational response corresponds to a magnetization motion, which can be characterized by a macroscopic parameter (such as the average magnetization direction) that remains in a single energy minimum, such as a nonhysteretic hard-axis loop. Switching corresponds to a motion in which the magnetization jumps from one energy minimum to another, such as a hysteretic easy-axis loop. More precisely, rotation corresponds to a motion in which no energy is dissipated in the magnetic system

in the quasi-static limit, whereas switching mandates an energy transfer into the magnetic system in the quasi-static limit. The situation is analogous to first- and second-order phase transitions. The distinction between rotation and switching becomes blurry when reversal is driven by large, fast, field pulses because in this situation the magnetic energy is far above any minima.

Rotational motions are, in general, easy to model and are robust. These motions are not strong functions of disorder or device shape. When a perturbing magnetic field pulse is applied to an in-plane magnetized thin-film device, the magnetization immediately starts to precess about the applied field direction following LL dynamics. This precession quickly causes the magnetization to tip into the out-of-plane direction, at which point a strong demagnetizing field oriented normal to the film surface develops. The magnetization begins to precess about the demagnetizing field, yielding a nearly in-plane rotation toward the applied field direction. Compared to the in-plane demagnetizing field, which is concentrated at device edges and corners, the out-of-plane demagnetizing field is relatively uniform across the device. As a result, dynamic motion is predominately a coherent rotational process. "Coherent" here does not mean that the magnetization is uniform. It means that the motion across the device is correlated and can be described by a single macroscopic parameter (or mode). Consequently, a single-domain model with LL dynamics and appropriately scaled anisotropies can provide a reasonable approximation of device behavior.

There are some differences between single-domain models and micromagnetics in small-field rotational response, particularly due to device edges or ends where magnetostatic fields are large. One example is shown in Fig. 13. In this study [46], a field pulse, with magnitude much smaller than the anisotropic and switching fields, is applied perpendicularly to the long axis of the stripe. Disturbed from equilibrium, the magnetization precesses about the long axis of the stripe. Micromagnetic simulations show that the central portion of the stripe precesses at a frequency close to that predicted by the single-spin model (9 GHz), but regions near the ends of the stripe precess at a lower frequency (3.5 GHz). It is also found that the end domain precessional frequency is more sensitive to part geometry than that of the central core. Another example of the distinct response of central and edge spins, presented in the next section, shows how large rotational pulses drive the device into saturation (Fig. 27).

Switching behavior, in which the system shifts from one energy minimum to another, is inherently more complex. Given that the magnetic system has many degrees of freedom, there are many ways in which the system can go "through" or "around" energy barriers. The type of switching process that occurs in a magnetic device is very dependent on the device shape, disorder, thermal fluctuations, and the temporal profile of the driving field [47,48,49,50]. It is important to distinguish between "switching" and "reversal" of magnetization. It is possible to reverse device magnetization by

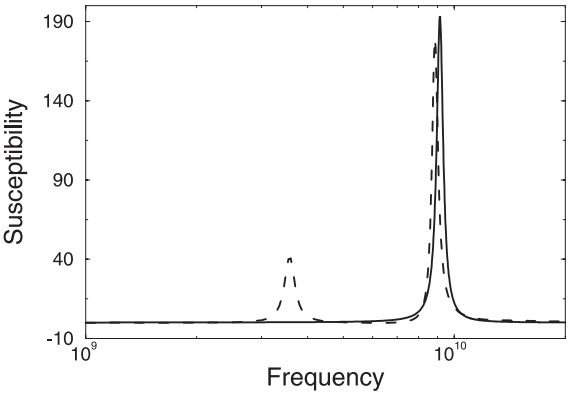

Fig. 13. Imaginary part of the susceptibility of a 1 μm × 50 nm × 5 nm Permalloy stripe, to a small field pulse applied perpendicularly to the long axis of the stripe. The one peak of the single-spin LL model (*solid line*) contrasts with results from a micromagnetic calculation (*dashed line*), which reveals the presence of end regions precessing independently of and more slowly than the central core

a rotational process. One such process would be to ramp up the hard-axis field to a value greater than that of the anisotropic field, rotate the applied field to the new magnetization direction, and then ramp down the the applied field amplitude. The value of reversing the device magnetization by a switching process is that the device is allowed to find its own low-energy path for reversal and the switching field is lower than that required for rotation. The disadvantage is that it may be less predictable and controllable.

For devices with large aspect ratios and blunt ends (such as in standard problem No. 4), the switching process usually starts at the device ends where the magnetostatic fields cause the magnetization to rotate off the easy axis in the quiescent state. In an easy-axis applied field, the magnetization at the device ends experiences a higher torque and rotates more quickly than the central part of the device. This results in the development of domain walls at the ends of the device, which propagate in and annihilate each other. Figure 14 shows the simulated magnetization in a 0.1 μm wide device in the process of switching by end-nucleated domain walls. If the ends of the device are tapered, the magnetization at the ends is pinned by the magnetostatic fields, the center of the device will reverse by a rotational process, and the reversal will propagate to the edges of the device. Figure 14 also shows a simulated magnetization plot of a tapered bit just after the central region has switched and before the ends have switched. If the system has strong disorder, then the switching mechanism may nucleate at a defect that creates a high angle moment and therefore, a large initial torque. The switching mechanisms listed above are for applied fields just above the quasi-static switching threshold. If large field pulses are applied, all moments will rotate rapidly and will reverse before any domain walls have a chance to form. In the limit

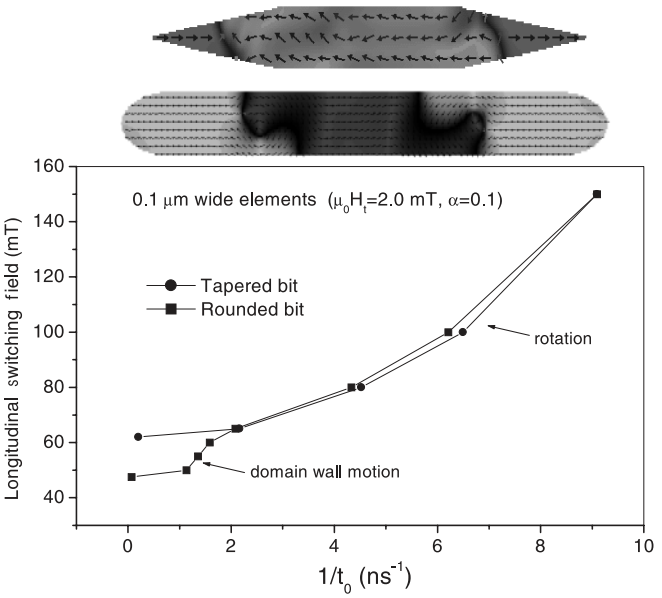

Fig. 14. Summary of OOMMF simulations of magnetization reversal in 0.1-μm wide rounded and tapered bits. The reversal is driven by a longitudinal step field pulse, and there is a small static transverse field component. The applied longitudinal switching field magnitude is plotted against the inverse reversal time, which is defined as the time between the onset of the field pulse and the sign change of the longitudinal magnetization. Also shown are micromagnetic structures of the bits during the reversal process

of large, fast, applied field pulses, all devices will reverse in a similar manner by a rotational process. This is shown in Fig. 14, which plots the magnitude of the reversal field versus the inverse of the reversal time (the reversal time is defined here as the time between the onset of the pulse and the time when the easy-axis magnetization reverses sign). For slow reversal times, one can see a difference in reversal characteristics for the two different device shapes corresponding to a rotation and domain-wall reversal process for the tapered and rounded bits, respectively. For short times and large applied fields, the magnetic bits behave the same.

In general, the exact nature of the reversal process near the switching threshold is very dependent on device shape, applied field geometry, and disorder. The desirability of a particular reversal mechanism depends on three factors: (1) low switching field to enable efficient writing of an element, (2) the reversal process must allow for bit selection, and (3) the reversal process must be predictable. Predictable means that there is little variation in the switching fields from device to device (which have been fabricated to be nominally the same) or for a single device switched many times. Achieving these desirable

reversal properties has been a challenge, and there are several possible routes for improvement: make the bits better single-domain particles; use domain walls or magnetization nonuniformities to enable low field reversal; or use high-energy rotational reversal and timing, rather than pulse amplitude, as a selection mechanism.

2.4 Modeling of Devices Based on Domain-Wall Motion

As just discussed, switching by domain-wall motion typically occurs by nucleation of a reversed domain followed by domain-wall motion. Once reversed domains are nucleated, the domains with low Zeeman energy grow at the expense of domains with higher Zeeman energy, and this growth is accomplished by motion of domain walls at the domain boundaries. Strictly speaking, as long as domain walls have nonzero width, domain-wall motion is a localized version of magnetization rotation where the rotation is confined to moving domain walls.

Many of the devices that have been considered consist of elongated rectangles or thin strips, so it is worthwhile to discuss the nature of domain walls in thin strips [51]. In a long strip of isotropic material, the magnetostatic energy is minimized when the magnetization lies in either direction parallel to the strip and "head-to-head" domain walls are formed at the boundaries between these oppositely directed domains.

Calculations that minimize the exchange and magnetostatic energy yield two simple forms for the head-to-head walls: transverse, and vortex walls. The transverse wall structure has minimum energy for thin, narrow strips, and the vortex wall structure has minimum energy for thicker, wider strips. These walls are illustrated in Fig. 15. The energies of the two structures are approximately equal when

$$w \cdot d \approx 130 \frac{A}{\mu_0 M_s^2}\,, \tag{9}$$

where w and d are the width and thickness of the film, respectively, and A is the exchange stiffness.

An alternative to nucleation and domain-wall motion can be found when the domain wall is preserved in the switching process and the domain wall can be nucleated by a suitable applied field or topological feature. Both memory and logic functions have been proposed by developing domain-wall circuits consisting of thin wires, loops, and topological structures to trap and store domain walls [52]. This type of technology has many parallels to concepts developed for bubble memory; however, it would be implemented with more conventional ferromagnetic metals.

One of the simplest domain-wall devices is the domain-wall-trap memory structure proposed by *McMichael* et al. [53]. One of the results of the calculations of head-to-head domain-wall structures is that the energy of a domain wall decreases if the strip is narrower. This makes it possible to construct

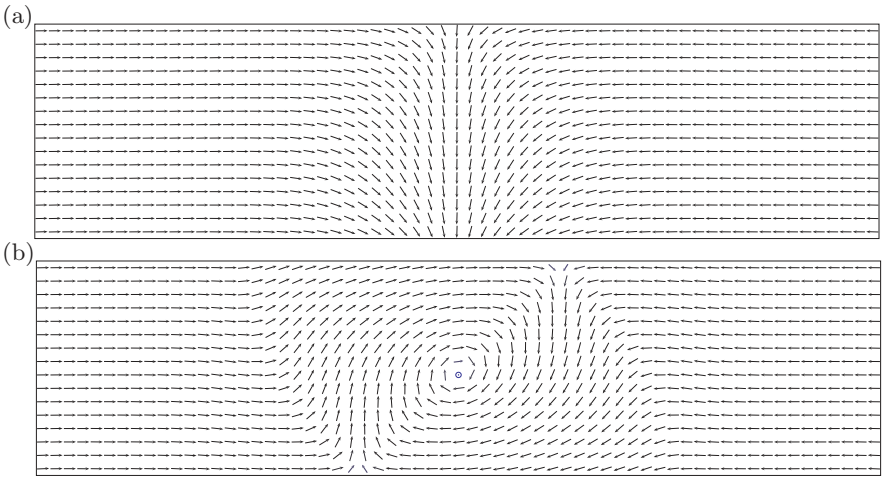

Fig. 15. (**a**) "Transverse" domain structure for a head-to-head wall calculated in a 2-nm thick, 250-nm wide strip of Permalloy, and (**b**) "vortex" domain structure for a head-to-head wall calculated in a 32-nm thick, 250-nm wide strip of Permalloy. Each arrow represents the magnetization of a subsample from 16 cells

an energy well for a domain wall by making a narrow section in the strip. A model "domain-wall trap" is illustrated in Fig. 16. The domain wall has minimum energy when it resides at the interior vertex of the device. The domain wall can propagate from one stable vertex position to another, thereby reversing the magnetization in the bridge region. The magnetization state can be read by making the domain-wall trap the free layer of a GMR or TMR device. The advantage of such a device is that the reversal energy is very low because, in a sense, much of the switching energy has already been provide by the trapped domain wall.

3 High-Frequency Magnetic Device Measurement

The development of smaller and faster magnetic devices for data storage has created a need for new types of high frequency magnetic device measurements. One must measure the magnetization response of individual submicrometer magnetic structures driven by subnanosecond magnetic field pulses or sinusoidal microwave magnetic fields in the 0.5 to 10 GHz range. The predictions of micromagnetic models, as described in the previous section, need to be investigated and validated. Fortunately, the same physical effects that give magnetic devices their utility, GMR and TMR, provide an ideal method for measuring a device's magnetic response. The electron transport relaxation times are very fast, of the order of picoseconds, making the device's resistance a good measure of its instantaneous magnetization state. In this section, we

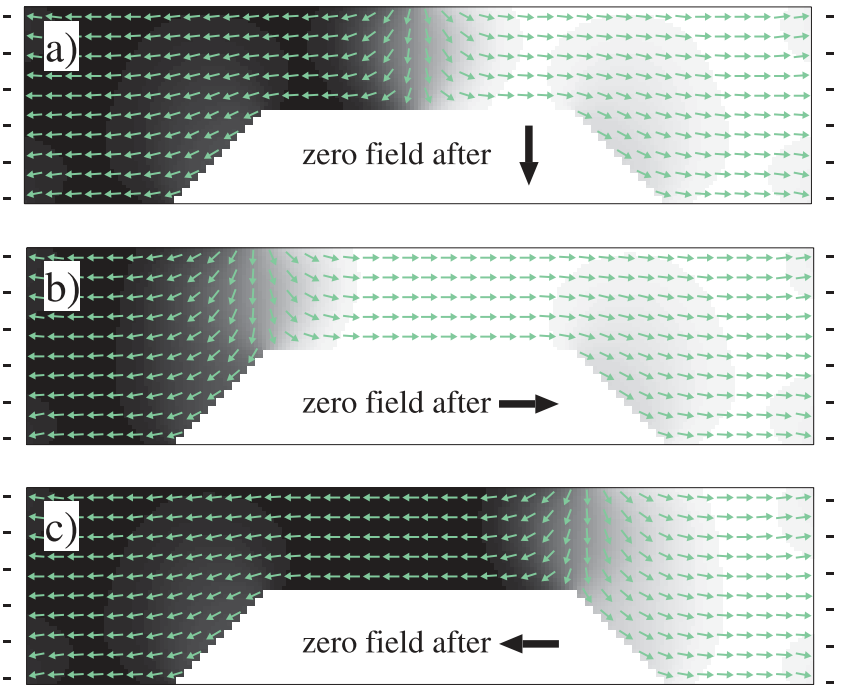

Fig. 16. Spin configurations of a domain-wall trap at zero applied field. The widths of the wide and narrow sections are 250 and 125 nm, respectively. (**a**) Unstable state after initialization in the −y direction. (**b**) and (**c**) Stable configurations after application of a field in the +x and −x directions, respectively

describe techniques for high-bandwidth excitation of GMR devices and high-bandwidth measurement of a device's resistance. These measurements can then be used to resolve the dynamic behavior of magnetization in devices.

Magnetoresistive devices can be incorporated into microwave circuits to provide high-bandwidth connections and magnetic field excitation. One configuration (shown in Fig. 17) consists of a GMR device connected to a 2-μm wide, 50 Ω microstrip transmission line called a sense line. The other end of the device is connected to ground, and so, the device effectively terminates the sense line. A constant current bias is applied to the device through the sense line. A change in the average magnetization orientation of the device's free layer changes the device's resistance which in turn changes the voltage across the device, as discussed in Sect. 1. This voltage step propagates along the sense line and can be taken off-chip for detection. The voltage change along the sense line is scaled down because of the voltage divider formed by device's resistance and line impedance. The change in voltage ΔV traveling along the sense line due to a change in resistance ΔR is given by $\Delta V = I(\Delta R)Z/(Z + R_i + \Delta R)$, where Z is the sense line impedance, R_i is

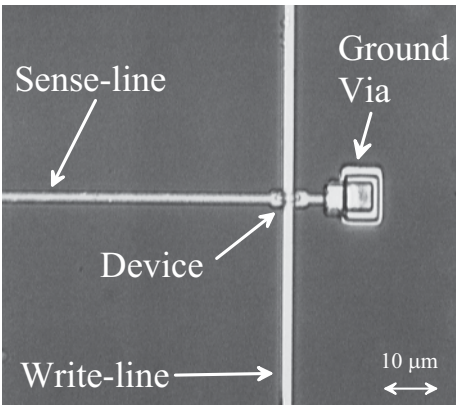

Fig. 17. SEM micrograph showing the microstrip write line and sense line. At the intersection of the lines is a spin valve device

the initial resistance, and I is the constant bias current. The actual measured voltage change is slightly lower due to losses along the line and reflections from impedance mismatches in the structure.

Another microstrip line lies directly above the device, separated by a dielectric layer. This line, termed the write line, serves as a high-bandwidth field source to the device. Figure 17 is a scanning electron micrograph showing both the sense line connected to the device and the write line over the device. The field from the write line, H, is estimated[9] by assuming a uniform sheet current across the microstrip and its image below the ground plane, which gives $H = V/(2Zw)$. Here, V is the voltage on the write line at the location of the device, $Z = 50\ \Omega$ is the impedance of the write line, and $w = 4\,\mu\text{m}$ is the width of the write line. Figure 18 shows voltage pulses, whose full widths at half maximum (FWHM) vary from 230 ps to 1 ns, that have traveled through the write line. Due to losses and dispersion along the line, the actual pulse amplitude at the device is greater than that measured at the end of the line. The device is located at the midpoint of the write line, and so, the voltage amplitude at the device is approximated by taking the average of the amplitudes measured with and without the write line in the circuit.

The combined test structure containing the device and the write and sense lines is fabricated from six layers deposited on a high resistivity ($\rho > 1000\ \Omega\,\text{cm}$) oxidized Si wafer. High-resistivity substrates are used to minimize high frequency losses due to currents induced in the substrate. Each layer is patterned by optical lithography to produce the proper waveguide structures and necessary vias. There are three metal layers separated by two dielectric layers. The GMR device sits on top of the first dielectric layer. The specific layer structure is shown in Fig. 19. The write line is a metal strip in the third metal layer, and the sense line is a metal strip in the second metal layer.

[9] Exact calculation of the magnetic field profile from the measured voltage profile is complex and requires detailed microwave modeling

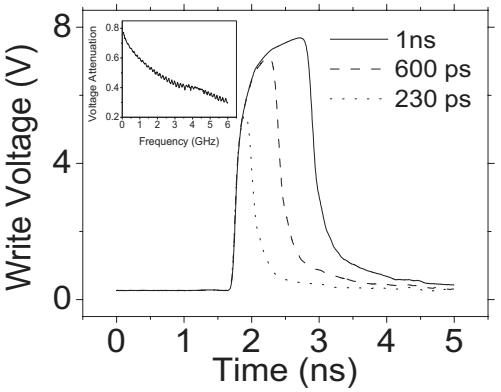

Fig. 18. Write pulses after traveling through the write line. The line bandwidth permits propagating pulses as narrow as 180 ps. The inset shows the typical frequency response of a write line. The lines are relatively lossy due to the small line widths

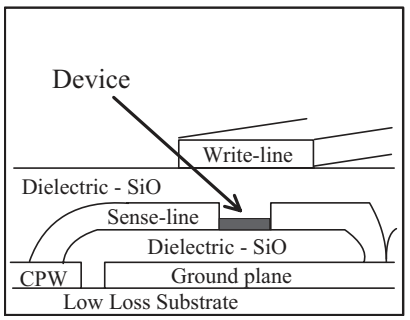

Fig. 19. Cross section of a high-bandwidth test structure

The first metal layer forms a ground plane that completes the microstrip structure for both lines. Each dielectric layer was 0.8-μm thick thermally evaporated SiO, which has a relative permittivity of approximately 6 [63].

The first metal layer also contains tapered 50-Ω coplanar waveguide (CPW) structures, that connect at their narrow end, to the microstrip lines through vias in the dielectric layers. The CPW center conductor width increases from 3 μm at the narrow end to 100 μm. These wide areas of the CPW serve as probe pads and allow high-bandwidth contact to external components by way of commercially available 40 GHz probes. An image of two complete test structures is shown in Fig. 20. The microstrip lines are visible and have connections to the CPW structures at their ends.

Both pulsed and continuous-wave (CW) excitations can be applied to the write line. For the experiments described here, a pulse generator is used that produces 50-ps rise-time[10] pulses with an amplitude of 10 V and a variable

[10] The rise-time is defined as the interval between 10 and 90% of the full amplitude on the rising edge of the pulse

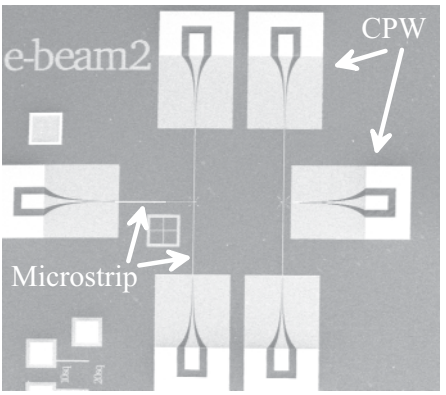

Fig. 20. SEM micrograph of complete high-bandwidth test structures. Image shows a 3 mm × 3 mm area

duration from 100 ps to 10 ns. The bandwidth limitations of the probe-station measurement, including the write line and all other cables and components in the field source path, increase the rise time to 100 ps and broaden the minimum pulse duration to approximately 200 ps. Figure 21 is a schematic representation of the measurement and shows the components along the field source (write-pulse) path as well as the device response (sense) signal path. A variable attenuator, which ranges from 0 to 81 dB in 1 dB steps, is placed at the output of the field-source and is used to vary the pulse amplitude. Additionally, two switches are placed in the field-source path (not shown in Fig. 21) that are used to reverse the current direction through the write line and hence the pulsed magnetic field polarity. Both the attenuator and the switches are broadband microwave components with a bandwidth of 0 to 40 GHz. After the pulse traverses the write line, it is taken off a chip to an oscilloscope to view. A CW frequency source, from a microwave oscillator or

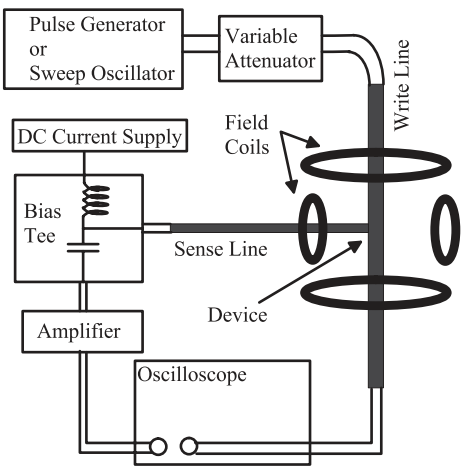

Fig. 21. Schematic of experimental high-speed measurement system

the output port of a microwave network analyzer, can also be used to drive the write line (see Sect. 4). However, it is important to note that for CW excitation, the power needs to be kept low to avoid heating the write line and it is hard to obtain as large a field amplitude as that obtained in the pulsed measurements.

As shown in Fig. 21, the 50-Ω port of a bias tee is connected to the sense line by way of a microwave probe attached to the sense-line CPW pad. A constant current bias is applied to the device through the inductive port of the bias tee, and the voltage measured across this port gives the dc resistance of the device in series with the sense line resistance and contact resistances. The voltage step associated with the resistance change of the device propagates down the sense line and is output through the capacitive port of the bias tee. This output is amplified and sent to an oscilloscope for time-domain detection or to a network/spectrum analyzer for frequency-domain detection. This path is shown in Fig. 21. The amplifier used here has a gain of 22 dB with a bandwidth of 80 kHz to 10 GHz.

In addition to the voltage response of the device traveling along the sense line, there is also a parasitic voltage signal induced by the capacitive coupling between the sense line and the write line. The coupling is about −80 dB, and for write pulses close to 10 V. This gives a 1-mV pulse whose shape is proportional to the derivative of the write pulse. Devices tested here generally have resistances of about 50 to 150 Ω with 4 to 10 Ω maximum resistance changes. This corresponds to a typical magnetoresistance signal of about 2 to 5 mV, which is significantly altered by the additional parasitic pulse.[11] The parasitic signal can be subtracted by taking a reference curve with write pulses applied while there is no current bias through the device or when the device magnetization is saturated by an external field. The device magnetization response is then given by the measured signal minus the reference signal.

Parasitic capacitive coupling can be useful in determining the position of the write pulse with respect to the sense response signal. In general, both the sense response and the write pulse are collected simultaneously on an oscilloscope. However, a relative delay is usually seen between the write pulse and the sense response because of cable length variations and different components along the two paths. The capacitive pick-up signal in the sense response path shows precisely the time at which the write signal turns on. The peak(s) in the parasitic signal can be compared to the peak(s) of the derivative of the write pulse signal to determine the actual delay. For frequency-domain measurements, background subtraction requires a full vector subtraction (real and imaginary parts) to account for the differences in phase between the background signal and the magnetic signal.

[11] The amplitude of the magnetoresistance signal is limited by the amount of current that the device can handle without significant heating. For a 0.5-μm wide device, this is a few mA

An important aspect of the apparatus is the type of detection system used. For the time-domain measurements described in this chapter, two types of oscilloscopes were used. One is a 1.5-GHz bandwidth oscilloscope capable of collecting single-shot waveforms with an acquisition speed of 8×10^9 samples per second. This type of measurement is useful in observing switching; the single-shot observation of switching events reveals unique properties of single switches that do not necessarily repeat from switch to switch (see Sect. 5). Unfortunately, the 1.5-GHz bandwidth falls just short of ferromagnetic resonance frequencies of magnetic thin films, and so, single-shot results may attenuate any precessional response and broaden the observed switching and rotational events. Increased bandwidth measurements can be taken by using a sampling oscilloscope. The sampling oscilloscope used in measurements described here has a bandwidth of 20 GHz, but this type of acquisition requires repetitive processes. The sampling technique acquires only one point within the time trace per event and captures the entire waveform by repeated sampling of points; each point is separated by a fixed delay in consecutive events. This method is useful for resolving high-bandwidth processes for repeatable, self-resetting events; for example, the small angle motion of the magnetization due to an impulse field along the hard axis (as presented in Sect. 4) can be measured in this manner. In this case, the damped oscillatory behavior of the magnetization is clearly resolved. Care must be taken when interpreting averaged measurements because features, such as slow response time, could arise from a distribution of magnetization responses and may not be representative of an actual single-event magnetization response.

The use of transport measurements to study the dynamic behavior of magnetic devices is a new area of research with few reported results [48,64,65,55,67,68]. Further improvements in this measurement technique can be made. A useful addition to the test structure would be including two perpendicularly-oriented write lines that allow field pulses along both the hard and easy axes. This kind of structure more closely resembles the cross-point architecture for MRAM operation [69] and allows measuring fully pulsed switching astroids that can be compared with the *Stoner–Wohlfarth* model [39]. An additional modification would be connecting the write line to ground immediately after the device. The short would create a voltage node and a current antinode at the device, thereby doubling the magnetic field and reducing the parasitic capacitive signal. The high-bandwidth measurement described here has, so far, been applied only to current-in-plane spin valves. Current perpendicular-to-plane tunnel junctions can similarly be fabricated within the test structure; however, there are additional complications due to the difficulty of impedance matching a high-impedance TMR device and to the presence of a parallel capacitance from the tunnel junction.

4 Rotation and Ferromagnetic Resonance in GMR Devices

Using the techniques described in the previous section, the high frequency response of magnetic devices can be measured in either the time or frequency domain. Figure 22a shows the response of a 0.8 μm × 4.8 μm spin valve subjected to a 180-ps transverse magnetic field pulse, and Fig. 22b shows the response of the same device to sinusoidal transverse microwave magnetic fields. The damped precessional motion is clearly seen in the time-domain data. These small-angle time-domain rotational data can be adequately modeled by single-domain LL models, provided that the measured, rather than calculated, anisotropy field is used [60]. The frequency-domain data clearly show

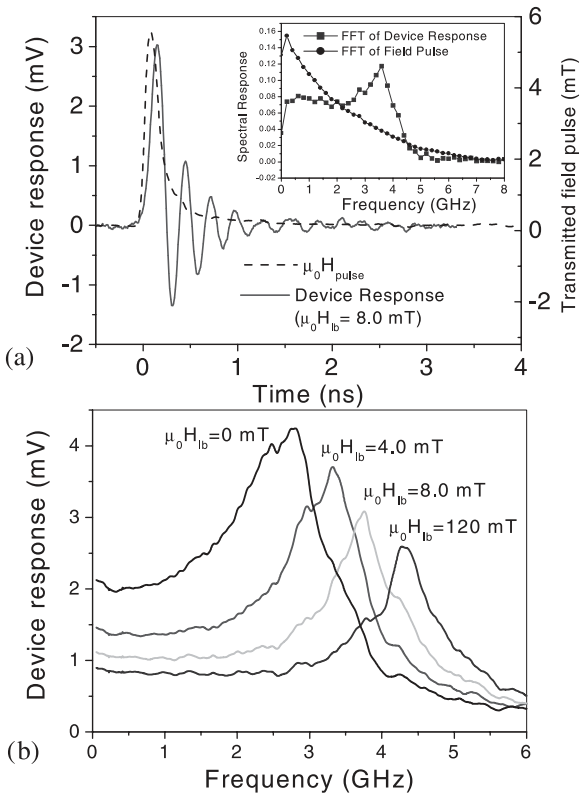

Fig. 22. (**a**) Magnetoresistive response of a 0.8 μm × 4.8 μm spin valve driven by a 180-ps transverse field pulse. The inset shows the Fourier transform of both the spin valve response and the applied field pulse. (**b**) The frequency response of the same device for a series of longitudinal applied fields. For the frequency-domain data, the write line was driven by 10 mW CW power which corresponds to a 3.1-mT peak field. The data is taken from [66]

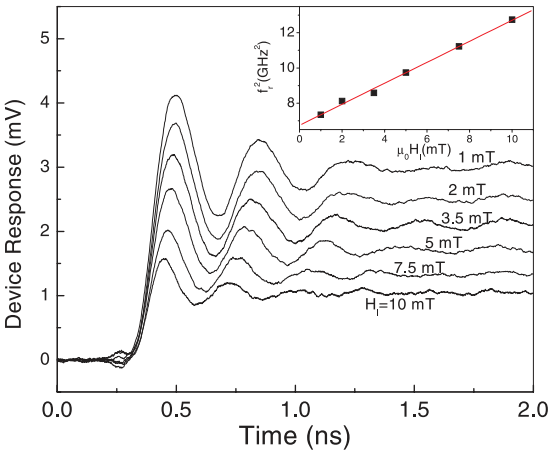

Fig. 23. Magnetoresistive response of a 0.8 μm×4.8 μm spin valve driven by a transverse step pulses for a series of longitudinal bias fields. The *inset* shows a plot of the resonant frequency squared versus the bias field amplitude, demonstrating good agreement with simple FMR models for uniform rotation

the FMR peak, which shifts to higher frequencies as the longitudinal bias field is increased. The position of the resonance can be adequately fitted by the simple Kittel resonance formula $f_r = \mu_0\gamma/2\pi[(H_l + M_s)(H_l + H_k)]^{0.5}$, where H_l is the applied easy-axis field and H_k is the agnetostatic anisotropic field. This can be seen in Fig. 23, which shows the precessional relaxation in response to a series of step pulses with different easy-axis bias fields H_l. The inset shows a plot of the square of the resonant frequency versus the longitudinal bias field and a straight line fit to the data. The slope of the fit yields the g factor, and the intercept yields the in-plane anisotropy field.

For small angle motion, time-domain and frequency-domain data are equivalent, and the device response is described by the frequency-dependent complex transverse susceptibility. The transverse susceptibility χ_t can be calculated from the time-domain data by normalizing the Fourier coefficients of the device's response by the Fourier coefficient of the applied field pulse. Alternatively, the transverse susceptibility can be calculated from the frequency-dependent device response by normalizing the device's response to the frequency-dependent field amplitude. Both techniques yield real and imaginary components of the susceptibility. However, for both techniques, there is some uncertainty in separating of the real and imaginary parts of the susceptibility, which corresponds to the difficulty in precisely measuring the relative phase of the drive and response at the device location, and it is easier to fit the amplitude of the susceptibility. The transverse susceptibility amplitude, calculated from time-domain and frequency-domain data, is shown in Fig. 24. Also shown is a fit using the single-domain LL model. The only adjustable parameter is the damping coefficient α which is 0.03 for this device.

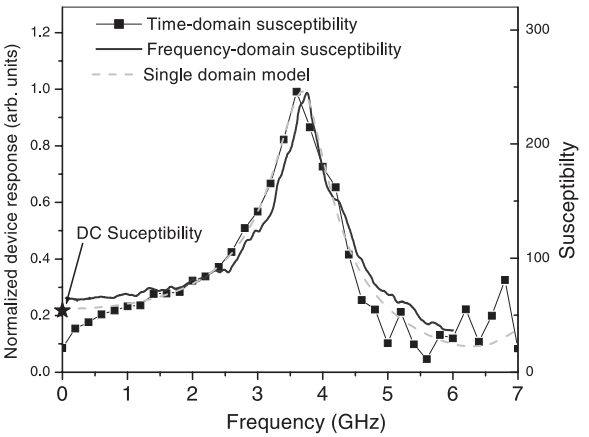

Fig. 24. The magnitude of the transverse susceptibility calculated for the time- and frequency-domain data shown in Fig. 22. Also shown is a fit using the numerically calculated susceptibility from a single-domain LL model. The only adjustable parameter in the fit is the damping constant which is determined as $\alpha = 0.03$ for this device, the data is taken from [66]

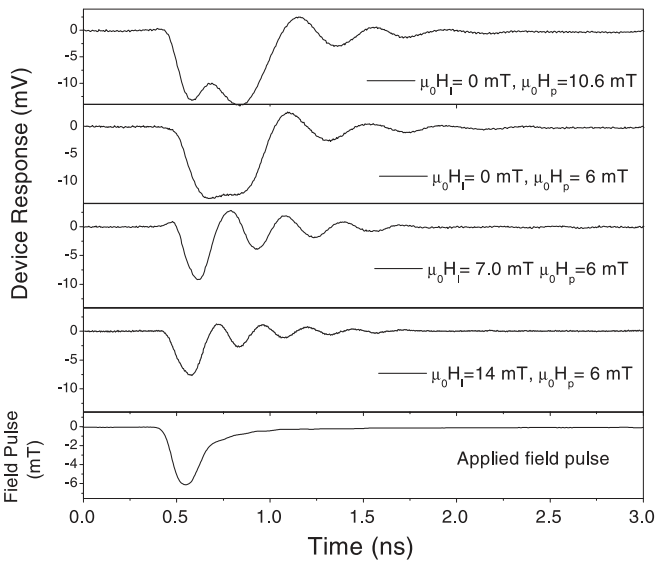

Fig. 25. Magnetoresistive response of a 0.8 μm × 4.8 μm spin valve driven by a 180-ps transverse field pulse. The bottom panel shows the applied field pulse. The next three frames above show the device's response with decreasing applied longitudinal bias fields. The top frame shows the response of the device, with no longitudinal bias field and a larger pulse-field amplitude, showing that the device's response is saturated

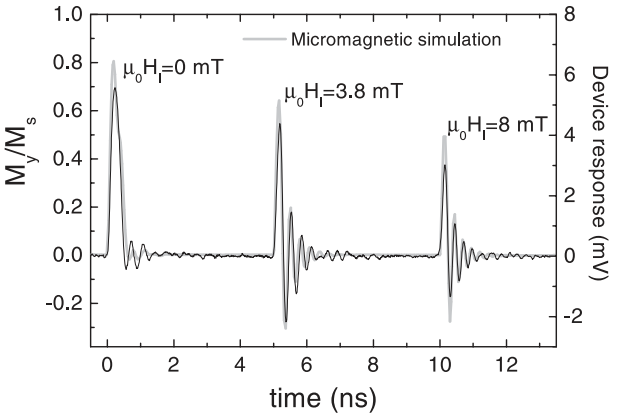

Fig. 26. Magnetoresistive response of a 0.8 μm × 4.8 μm spin valve driven by a 180-ps transverse field pulse for several values of longitudinal bias field (the *scale* is on the *right axis*). Also shown is the dynamic response of transverse magnetization calculated by using a micromagnetic simulation (the *scale* is on the *left axis*). The only adjustable parameter is the damping constant, which is 0.03 for this simulation. Note that the micromagnetic model provides a reasonable fit for the whole range of data

The time-domain response of a spin valve for several values of the longitudinal bias field H_l and pulse amplitude is shown in Fig. 25. The data correspond to an impulse response in which the field-pulse width (180 ps) is much shorter than the device's response time. The response for large longitudinal bias fields shows small angle precessional relaxation, as previously described. As the magnitude of the longitudinal bias field decreases, the resonant frequency decreases, and the amplitude of the response increases. When there are no longitudinal bias fields, the device saturates as shown by the lack of increased device response when the pulse amplitude is increased, as in the top frame of Fig. 25. The data near saturation cannot be adequately fit using single-domain models; however, micromagnetic simulations provide a reasonable fit to the data over the whole range of longitudinal bias fields, as in Fig. 26. The only adjustable parameter in the micromagnetic simulation is the damping parameter.

The response of the spin valve to transverse fields above the saturation field shows a double peak structure, which indicates that the magnetization overshoots its equilibrium position. Figure 27 shows a micromagnetic simulation that describes the observed response. The magnetization rotates into the transverse direction when the transverse field pulse is applied, but the field pulse is turned off before the device magnetization has a chance to relax fully to its equilibrium value. Specifically, there is a small magnetization component along the z axis when the field pulse is turned off. This component contributes a perpendicular magnetostatic field that causes the central por-

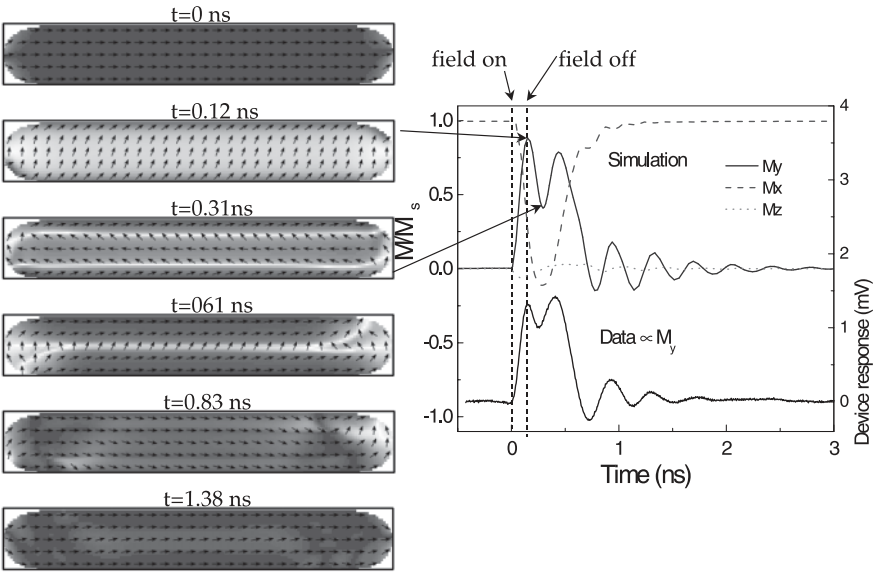

Fig. 27. High-angle rotation in an 0.8 µm × 4.8 µm spin valve ($\alpha = 0.02$, $H_p = 80\,\text{mT}, 150\,\text{ps}$, $H_l = 0\,\text{mT}$). The *top plots* shows a OOMMF simulation, and the *bottom plot* shows experimental data (which is proportional to M_y). The field pulse is sufficient to saturate the free-layer magnetization along the y axis. The pulse turns off before the magnetization has fully relaxed, leaving residual magnetostatic fields that cause the magnetization to rotate into the negative x-direction after the pulse is turned off

tion of the device to rotate 180° when the applied field is turned off. In this case, the residual demagnetizing fields are not sufficient to rotate the edges of the devices, the edges pull the center of the device back to the original direction, and the device does not switch orientations. These types of dynamic effects, which can cause device reversal, will be discussed in the next section.

5 Switching of Small GMR Devices

Precise control of magnetization reversal in patterned magnetic structures and devices is critical for the successful operation of MRAM [69] and continues to be a significant challenge. Measurements, using quasi-static variation of magnetic fields to drive switching, have clearly shown complex micromagnetic structure during the switching processes of these structures [70,71,72]. For MRAM to become a competitive technology, however, it must be able to operate at frequencies near and above 1 GHz. This means that individual bits (devices) must be written (reversed) using applied field pulses whose duration will be of the order of one nanosecond, with the added requirement that the full reversal of the magnetic device occurs within the same time frame.

The high-speed reversal process will be very different from the slow quasi-static switching processes conventionally studied. The high-bandwidth electrical measurement technique, described in Sect. 3, provides a useful method for measuring the device reversal properties in response to a range of pulse amplitudes; duration varies from a few nanoseconds down to about 200 ps. Looking at the remnant state of the device after a series of field pulses can yield the critical values of pulse parameters, amplitude, and duration that are required for reversal to occur. These data can give insight into the reversal process. Further, observation of the time-dependent resistance during the switching process can give direct information on the precise sequence of states that occur during reversal. This section will present both remnant and real-time resistance data for high-speed switching in micrometer-sized spin valves. We will also describe a novel method for magnetization reversal in spin valves driven by hard-axis field pulses in which the switching probability is determined by the precessional motion of the magnetization.

It is clear that a single-domain model with an in-plane, uniaxial energy surface (as shown in Fig. 5) cannot accurately describe the switching behavior of most submicrometer magnetic devices. It remains a great challenge to fabricate a magnetic device with ideal single-domain behavior. However, it is not clear that single-domain behavior is required or desirable for magnetic memory applications. What is needed is a bistable device that can be switched between its stable states efficiently (low switching field), controllably (predictable and reproducible switching fields), and fast. An example of a bistable spin valve device was shown in Fig 3. Though it is not accurate to think that the device is uniformly magnetized during the reversal process, it is convenient to consider that the device state is described by a macroscopic variable, such as average magnetization, or magnetization angle (θ), and to consider the energy as a function of this macroscopic state variable. Disorder alters the device energetics from the ideal, single-domain case, shown in Fig. 5a. The actual energy surface must still contain two global energy minima, one with the average magnetization direction at $\theta = 0$ corresponding to the low resistance state and the other at $\theta = \pi$ corresponding to the high resistance state; however, there may be considerable disorder in the barrier separating these two states, as shown in Fig. 28.

Application of an easy-axis field lowers the energy of one well with respect to the other and reduces the barrier height between the wells. In a field H^*, which we define as the critical field amplitude,[12] the barrier becomes completely suppressed allowing a fully dynamic magnetization reversal process. In this case, a switch occurs if the field duration is sufficient for the magnetization state to evolve just beyond where the barrier maximum would be in zero applied field. This is shown schematically in Fig. 28. Panel (a) is a sketch

[12] H^* is the quasi-static switching field at $T = 0$. However, at finite temperature, the quasi-static switching field is less than H^* because the magnetization may reverse by a thermally activated process

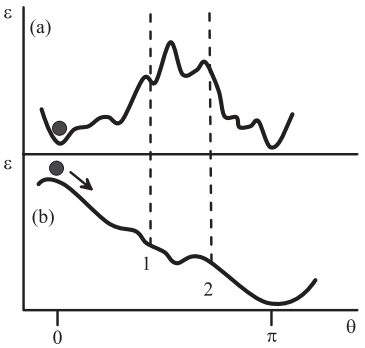

Fig. 28. Hypothetical disordered energy surface for the magnetization state as a function of in-plane angle θ. (**a**) Energy surface for zero applied field. (**b**) Energy surface for applied easy-axis field larger than H^*

of the hypothesized energy surface, for the magnetization state in zero applied field, that has a uniaxial character with some disorder built in. Panel (b) shows the energy surface in an applied easy-axis field $H \geq H^*$. While the field H is applied, the magnetization state will evolve toward reversal. If the magnetization is at point 1 when the field turns off, the energy surface reverts to what is shown in panel (a), and the magnetization will relax under the influence of internal fields toward the global minimum at $\theta = 0$. If the magnetization evolves to point 2 when the field turns off, then the magnetization will complete a successful switch and relax to a minimum near $\theta = \pi$. Because of disorder, the system may get temporarily stuck in a local minimum, leading to a long-lived metastable state.

In general, the rate at which the magnetization evolves should increase with increasing torque, which in turn is proportional to the applied field. Thus, for fields above H^*, larger applied fields require shorter pulse durations for a switch to occur. We define the critical pulse duration δt^* as the minimum duration required at a given field value for a switch to occur. We expect $(\delta t^*)^{-1}$ to increase with field amplitude; however, the exact functional form depends on how the rate of magnetization change increases with the applied field. This depends on the reversal mechanism. Knowledge of this dependence is especially useful for optimizing fast-pulsed MRAM programming.

The high-bandwidth magnetoresistance technique has been used to measure δt^* as a function of reversal field for submicrometer spin valves. In particular, we show results for a $0.9\,\mu\text{m} \times 4.2\,\mu\text{m}$ spin valve with a 2.5-nm thick free layer consisting of 1.0 nm Co and 1.5 nm $Ni_{80}Fe_{20}$. The device was bistable with a resistance change between states of 4.1 Ω. The low-resistance state of the device was 81 Ω, which gives a corresponding GMR of 6.3% after the contact resistance is subtracted. This device was fabricated within the test structure described in Sect. 3, and the orientation of the device was such

that the field from the write line was oriented along the easy axis. A 2.5-mT transverse (hard-axis) bias field was added to aid the switching process.

Repeated measurements of the device response to nominally identical reversing field pulses show that, for certain combinations of pulse field and amplitude, the device exhibits multiple remnant state outcomes. Such outcomes include complete reversal, a return to the initial state, or some intermediate states with resistances between those of the parallel and antiparallel spin valve states. These intermediate or metastable states indicate the presence of disorder as mentioned above; the disorder provides the pinning of long-lived micromagnetic structure within the device. For the measurement, the probability of switching to various states was determined from the result of 100 events in which the device was subjected to nominally identical field pulses, the remanent state was read, and the device was reset by a 1-s long, 15.0-mT external field directed in the initial magnetization direction. Figure 29a shows the distribution of final-state outcomes for the device in response to 445-ps duration[13], 16.6-mT field pulses. For this field pulse, the device switches half of the time, occasionally ends up in a metastable state with 75% of the magnetization switched, or the device does not switch at all. The pulse amplitude, 16.6 mT, exceeds $H^* \approx 9.8$ mT for this device. Figure 29b shows the time-dependent, easy-axis magnetization (calculated from the observed magnetoresistance signal) for each of the three observed outcomes. It takes 1.1 ns for the device to complete a switch, meaning that most of the magnetization change occurs under the influence of internal fields

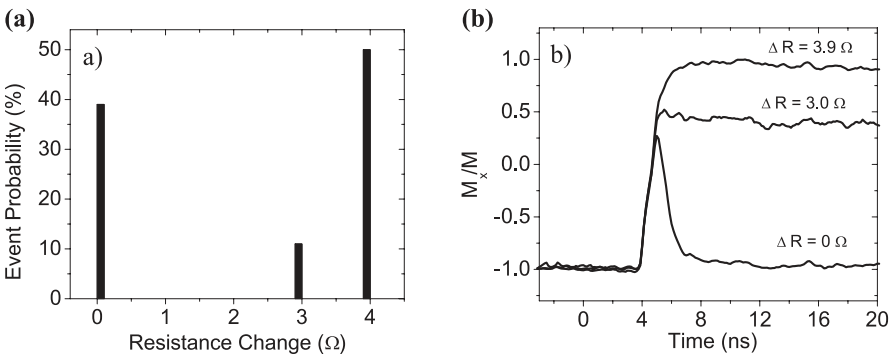

Fig. 29. Spin valve response for the device described in the text to 16.6-mT, 445-ps field pulses. (**a**) Histogram showing measured distribution of remnant state outcomes: 0 Ω-no change in state; 3 Ω-partial reversal; 4 Ω-full reversal. (**b**) Time-resolved MR signal showing switching responses for each outcome exhibited. M_x/M is the easy-axis component of the average magnetization normalized to the initial-state magnetization

[13] Here, pulse duration refers to the FWHM of an approximate Gaussian-shaped field pulse with a 100-ps rise time and a 300-ps fall time

after the applied field strength has diminished. Even when the device did not switch, a significant motion of magnetization occurred. In this case, the field is not on long enough for the device to complete the switch.

The probability of switching to the various states was collected for a series of pulse-duration values holding the pulse amplitude fixed[14]. The summary of these results is shown in Fig. 30. The probability will occur the three possible outcome states observed that is plotted versus the pulse duration. The complete-switch probability has a monotonic increase from 0 to 1 as the pulse duration increases by about 60 ps; δt^* for this amplitude, which we determine as the point where the full switch probability is at least 98%, is 480 ps. Furthermore, δt^* was determined in the same manner for a series of field values to produce a plot showing the relationship between the critical-pulse duration and the field amplitude. This plot is shown in Fig. 31. The quasi-static switching field is included to show the region where switching occurs by thermal activation over the barrier [73,74]. As expected, $(\delta t^*)^{-1}$ increases with the field amplitude; the amplitude required at 230 ps is almost a factor of 5 larger than that of the quasi-static switching field. However, the shape of the critical-pulse-duration curve is not linear. There are two visible kinks in the curve. One corresponds to the transition from thermal activation to dynamic reversal. The other, which occurs at higher fields, indicates a change in the nature of the reversal mechanism. OOMMF simulations (discussed in Sect. 2.3) were done to examine the dependence of the critical-pulse duration on amplitude. The simulation results also showed a kink in the plot

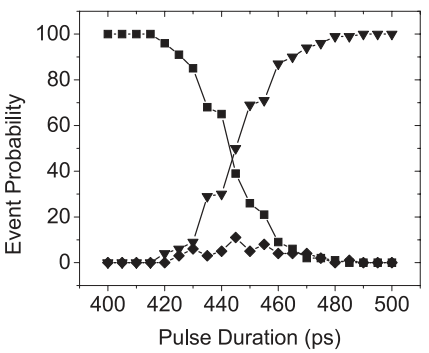

Fig. 30. Probability of switching to various outcomes as a function of pulse duration in a fixed field (measurements were made on the same device characterized in Fig. 29). *Squares* indicate no switch, *triangles* indicate full switch, and *diamonds* indicate a metastable state. Here, for 16.6-mT fields, the critical-pulse, duration for switching is 480 ps

[14] Due to the bandwidth limitations of the write line, there is a slight increase in pulse amplitude with duration of about 1.5 mT per 100 ps. This has been accounted for in the data presented in Fig. 31

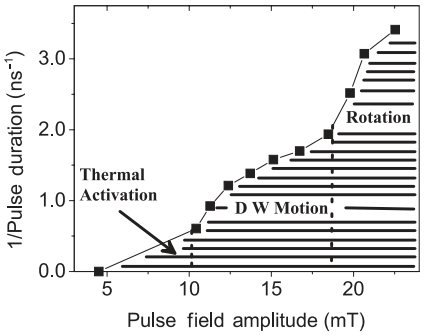

Fig. 31. Inverse critical-pulse duration as a function of easy-axis field amplitude. Shaded area on the plot indicates a favorable combination of pulse amplitude and duration for switching. The *vertical dotted line* separates regions where the switching mechanism differs

of inverse critical-pulse duration versus field. The kink occurs in a field where the reversal mode changes from predominantly domain-wall motion to one dominated by the rotation of magnetization in the center of the bit.

The observation of magnetization during the reversal process provides further evidence that changes in the reversal mode occur in higher fields. Figure 32 shows the time-resolved magnetoresistance signal during the reversal of a device in response to 10-ns easy-axis field pulses. The magnetoresistance signal is proportional to the easy-axis component of the average magnetiza-

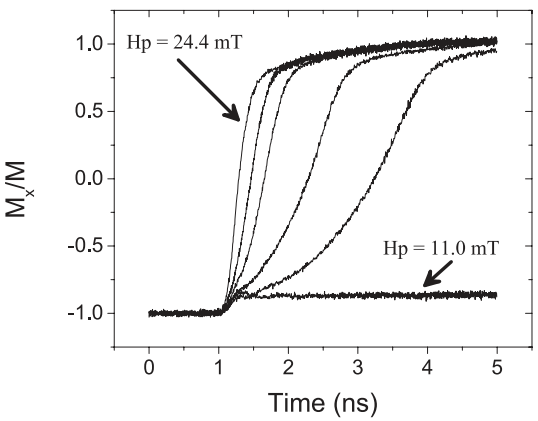

Fig. 32. Time-resolved magnetoresistance change during a spin-valve reversal process. An easy-axis field pulse with a 10-ns duration was applied. The pulse amplitudes for the curves shown (*left to right*) were 24.4 mT, 18.9 mT, 16.6 mT, 14.5 mT, 12.6 mT, and 11.0 mT. No reversal occurs for the lowest applied field (H_p), and the reversal time decreases as the applied easy-axis field increases

tion. For the lowest applied field pulse, the device shows a small response but does not reverse. This pulse amplitude is above the quasi-static switching threshold, and the device would reverse by thermal activation if the pulse were left on for a long time (several seconds). All of the other traces on the plot show full reversals, and the time it takes to reverse decreases as the applied field amplitude increases. There is a distinct transition between the two slowest reversals and the three fastest reversals, indicating transition from domain-wall motion to a rotational reversal mechanism. Note that none of the reversal events, even the high field events, show any coherent precessional relaxation, as predicted by single-domain models and as observed in the rotational motion presented in Sect. 4. This will be discussed further in Sect. 6 when the effects of disorder are studied.

The results show that spin-valve magnetization can be reversed by using sub-nanosecond pulses at the expense of larger required field amplitudes. In addition, single-shot measurements show the existence of metastable states. The existence and nature of these states, though interesting from a fundamental point of view, present a reliability problem for MRAM. Magnetization reversal in response to subnanosecond pulsed fields is particularly susceptible to incurring metastable states if the pulse turns off when the magnetization is in a high-energy state. This occurs because the relaxation of magnetization occurs under the influence of disordered internal fields that allow the magnetization configuration to sample various small, local minima (metastable states) within the energy surface (see Fig. 28). The final magnetization state will depend sensitively on the field amplitude and duration, as well as on damping mechanisms and temperature. In contrast, longer duration fields forces the magnetization to relax into the absolute minimum while the field is on.

Two kinds of metastable states have been observed. The first group consists of near-switched states whose resistances differ by no more than 10% of the actual high- or low-resistance state. Although these states are discernible, their occurrence in response to a reversing field is categorized as a full switch because it is safe to assume that the barrier to switching has been fully overcome and the final magnetization configuration is very close to that of the intended state. Measurements on $0.9\,\mu\text{m} \times 4.2\,\mu\text{m}$ spin valves have shown [65] that the probability these states occur does not vanish but rather oscillates as the field amplitude increases. Figure 33 shows a plot of the switching probability versus pulse amplitude for various pulse durations. For 10-ns pulses, the probability as switching remains constant at 100% for fields above H^*. However, for pulse durations less than one nanosecond, the probability of completely switching shows significant fluctuations as the field is increased. Each decrease in complete switching probability is coupled with an increase in the probability of encountering a metastable state that has a resistance value differing by either 0.5 or 0.15 Ω from the fully switched state. The temporal evolution of the switches to states that differ by a few

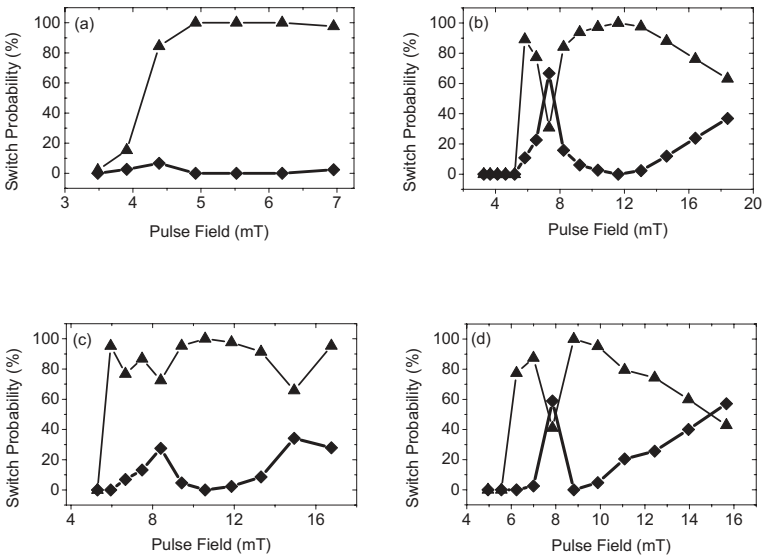

Fig. 33. Probability of complete switches (*triangles*) and near-switch metastable states (*diamonds*) versus field amplitude for fixed pulse duration. (**a**) 10-ns pulses. (**b**) 0.8-ns pulses. (**c**) 0.6-ns pulses. (**d**) 0.4-ns pulses

tenths of an ohm appears identical during the switching motion itself, indicating that the difference occurs in the relaxation process after the applied field is off.

The other group of metastable states consists of those with resistance between, but not close to, the two stable states. This indicates that the magnetic structure gets trapped in a long-lived, nonuniform or multidomain structure that is far from that of the stable states. For example, the histogram in Fig. 29a shows such a metastable state whose resistance indicates that 25% of the device has not reversed. As shown in Fig. 29b, the device settles into the metastable state directly during the reversal rather than first reversing completely and then later relaxing into the metastable state. Figure 34 shows the reversal response of another device that encounters a metastable state halfway through the switch. Each plotted response is due to nominally identical 5.8-mT field pulses. The duration of the field pulses is 0.9 ns, which is close to the critical-pulse duration. Each time, the device eventually reversed completely from the high- to the low-resistance remanent state. However, the time spent in the metastable state varied from less than 1 ns to more than many hundreds of nanoseconds. In this case, the height of the energy barrier to switching out of the metastable state was low enough to permit thermally activated escape at room temperature. The time-resolved response to higher amplitude field pulses (7.3 mT) with the same pulse duration did

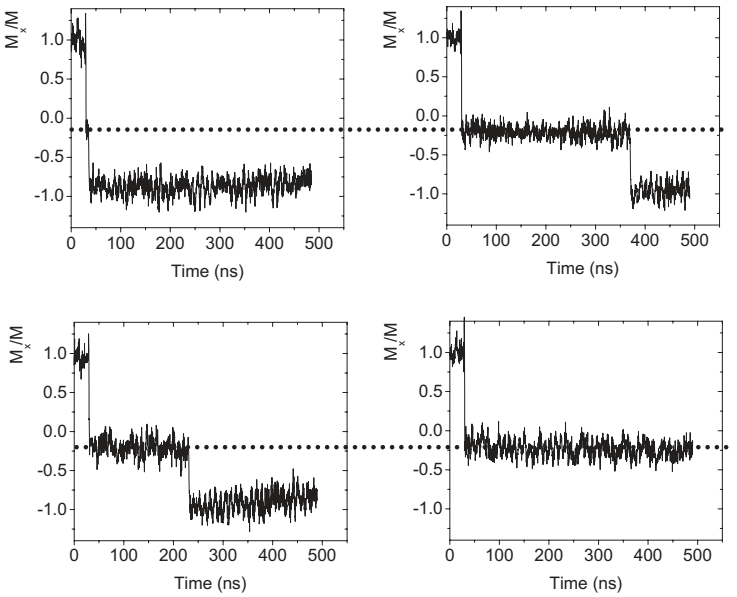

Fig. 34. Time-resolved magnetoresistance traces of switching through metastable states; each is a response to a 0.9-ns, 5.8-mT field pulse

not show any metastable state structure during the reversal process. At such high pulse amplitudes, the magnetization state evolves past the metastable configuration during the application of the pulse and results in a fast, clean switch after the applied field has decreased.

The data presented here indicate that the reversal of a bistable magnetic device in the dynamic regime (using short-duration field pulses with an amplitude much larger than the critical switching field, so that the energy is well above the undulations in the potential barrier) occurs faster and is less likely to enter a metastable state in which a significant portion of the device has not switched. However, desirable reversal processes (as discussed in Sect. 2.3) must allow for bit selection, and applying large field pulses will reverse the desired bit and also neighboring bits. One method for producing a reliable reversal process in the dynamic regime is to apply hard-axis field pulses and to use the natural resonance properties and pulse timing for bit selection. Reversal is possible in this case [75,76] if the field-pulse duration is much less than the time required for the dynamic motion of the magnetization to relax. A fast rise-time ($\leq$ 100-ps) pulse of sufficient amplitude causes the magnetization to overshoot the hard axis during its precessional trajectory. If the field pulse terminates when the magnetization has just overshot the hard axis, the internal fields of the device will cause the magnetization to reverse. This process is shown schematically in Fig. 35, which is a plot of the

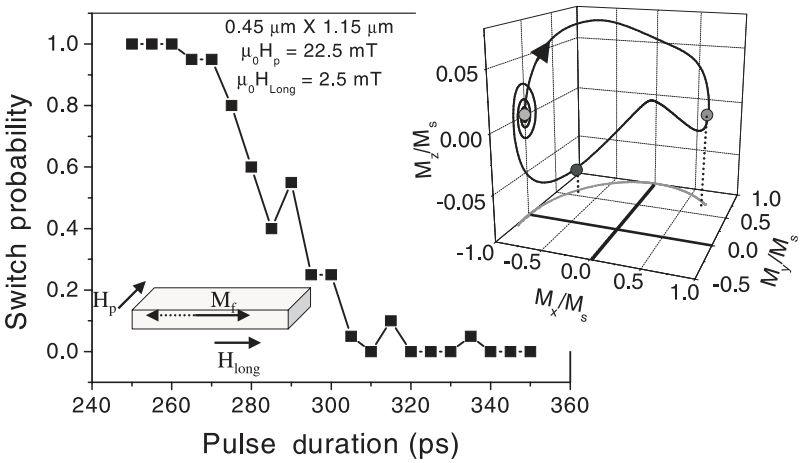

Fig. 35. Switching probability as a function of hard-axis pulse duration for the same device shown in Fig. 36. The *inset* shows a calculated trajectory that illustrates the dependence of switching on pulse duration. For short pulse durations, magnetization has an opposite easy-axis magnetization when the pulse is turned off, leading to magnetization reversal. For long pulse durations, the magnetization precesses back into the original easy-axis direction, and the device does not switch

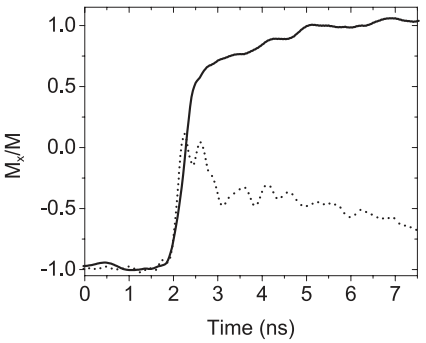

Fig. 36. Time-resolved MR signal for a 0.45 μm × 1.2 μm device driven by a hard-axis field pulse. The response to a 230-ps pulse is given by the solid curve and is a switch. The response to the 325-ps pulse is given by the dotted curve and is a no-switch

calculated trajectory of the magnetization of a small spin-valve device. For a 0.45 μm × 1.2 μm device, it was determined by measurement that this occurs consistently for pulses whose duration is less than 260 ps. The switching probability, as shown in Fig. 35, decreases to zero for wider pulses, which is consistent with precessional motion where the magnetization swings back toward the initial magnetization direction. Figure 36 shows the measured temporal evolution of magnetization that exhibits reversal for a short pulse

(230 ps) and nonreversal for a wider pulse (325 ps). Note that, for the wider pulse where there was no reversal, the magnetization takes a long time to relax back to the initial state because the pulse terminates when the magnetization is rotated close to the hard axis and magnetization relaxes only in the presence of internal fields. This again illustrates the importance of pulse timing in determining the reversal process. This type of precessional reversal, using hard-axis pulses, is potentially useful because it drives a single reversal mode (uniform rotation) and it relies on precessional motion and timing (which is easier to control than barrier height and shape) to determine the reversal process.

6 Effects of Disorder and Thermal Fluctuations

In this section, we discuss the effects of magnetic disorder and thermal fluctuations on magnetic device dynamics. Magnetic disorder can arise from many sources such as edge roughness, random local anisotropies, and disorder in interlayer couplings. This disorder has important consequences for the dynamic response of magnetic devices. Several examples of the effects of disorder on magnetization dynamics were shown in the last section, including the presence of long-lived metastable states and variability in the reversal process. Thermal fluctuations of the magnetic system, which are always present, play an increasingly important role as device dimensions are scaled down. Near the critical switching threshold, switching events are driven by thermal activation processes. For slow quasi-static switching, magnetization reversal occurs in this critical regime and is therefore always thermally driven. Local defects can combine with thermal fluctuations to cause fluctuations of small magnetic regions of the order of tens of nanometers, giving rise to low frequency $1/f$ voltage noise. As the device size is scaled down, these fluctuating regions become an increasingly large fraction of the device, and the voltage noise increases. Further, as the device size is scaled down, thermal fluctuations in the entire device volume become important and give rise to high-frequency noise in the GHz range.

6.1 Effects of Disorder

The effect of disorder on magnetization rotation of a spin-valve device can be seen in the micromagnetic simulations shown in Fig. 37. The disorder, which in this case is due to edge roughness and small (5 nm) voids, causes a slight increase in damping for large magnetization motions. In this case, the disorder is weak and does not qualitatively change the magnetization response of the device. The disorder creates short-wavelength spin waves as the magnetization rotates, which can clearly be seen in the image of $\boldsymbol{H}(\boldsymbol{r})$ within the magnetic element. The magnetic field, $\boldsymbol{H}(\boldsymbol{r})$, is proportional to the divergence of the magnetization and shows the generated spin waves

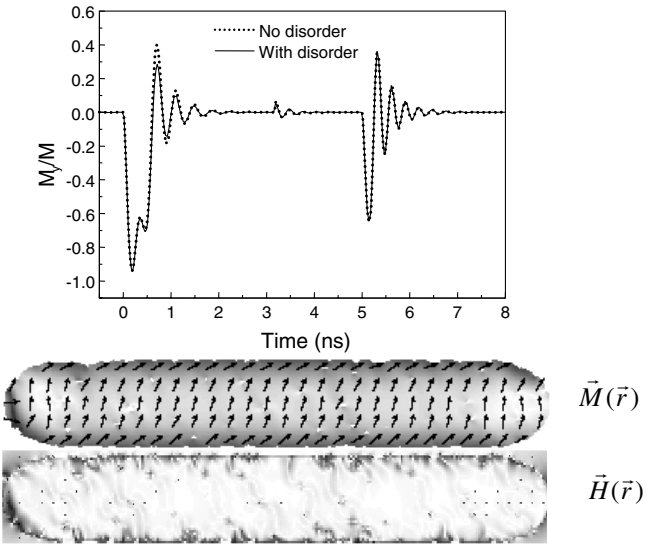

Fig. 37. Micromagnetic simulation of a spin-valve device driven by a hard-axis field pulse with and without disorder. The device size is 0.8 μm × 4.8 μm, and $\alpha = 0.03$. The response with larger amplitude is for the device with no disorder

more clearly than the plot of the magnetization because the deviations in magnetization are quite small.

If the disorder is larger, the qualitative nature of the magnetization response will be changed. This is seen in Fig. 38a, which shows the simulated response of a 0.4 μm × 0.8 μm magnetic device to a 200-ps transverse field pulse. In this case, strong random anisotropy is added to each cell. As seen, the coherent precessional relaxation is suppressed, and the system breaks up into a disordered state in which many spin-wave modes are present.

The effects of disorder are more important when a magnetic device is switched between two easy-axis magnetization states. Figure 38b shows a switching event in the same device discussed in Fig. 38a. The disorder more completely suppresses the coherent precessional relaxation after a switch. Strong disorder makes the switching event chaotic, and the magnetization breaks up into irregular, nonuniform magnetization patterns during the tail end of the switching process. This shows up as a broad relaxation tail in the easy-axis magnetization. The measured magnetization dynamics during switching of spin-valve devices (see Fig. 32) does not show coherent precessional relaxation and qualitatively resembles the simulations shown in Fig. 38b. This suggests that there is considerable disorder in real devices.

The amount of disorder in magnetic devices is not well understood, and it is very difficult to measure experimentally. To characterize the effects of disorder fully on high-frequency device dynamics, one would need to resolve magnetic structure on a 5-nm scale and a 20-ps timescale. However, disor-

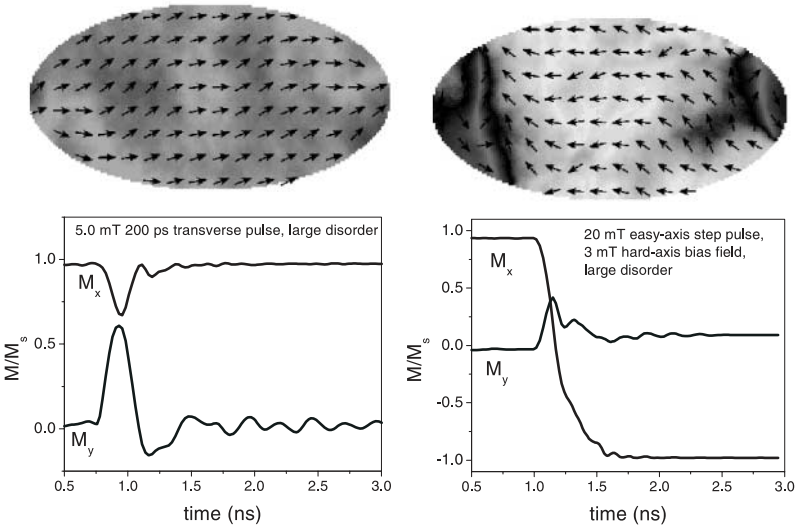

Fig. 38. OOMMF simulations of a $0.4\,\mu\text{m} \times 0.8\,\mu\text{m}$ MRAM device in the presence of large random anisotropy ($\alpha = 0.02$). (**a**) Rotational response driven by a hard-axis field pulse. (**b**) Switching response driven by a longitudinal field pulse

der can have important consequences for device operation, particularly for MRAM switching. For switching, a single defect can dramatically change the switching threshold of a device. Further, disorder can cause long-lived metastable states, as observed in the previous section. Noted that micromagnetic simulations still cannot predict the long-lived metastable states that are observed in real devices. This indicates that micromagnetic simulations do not include the proper type of disordered magnetic structures found in real devices and do not include all of the important physical effects, such as thermal activation or the ability to simulate over a wide range of timescales.

One method for examining disorder in magnetic devices is characterizing the low-frequency magnetic noise. Defects can create locally perturbed magnetization states that may have several stable configurations. The magnetization around these defects can fluctuate due to thermal activation. The fluctuation in magnetization in an active GMR device appears as voltage noise. If there is a broad spectrum of activation energies, then the noise spectrum is $1/f$. $1/f$ noise in GMR devices have been studied by several groups [77,78,79,80]. In small devices, the noise often can be resolved into a series of two-level fluctuators. Information on the size and moment of fluctuations can be obtained by studying their temperature-dependent switching times, [78]. Fluctuations often involve regions a few tens of a nanometer in diameter.

6.2 Effects of Thermal Fluctuations

In addition to disorder-induced low-frequency magnetic noise, there are intrinsic thermal fluctuations of the device's magnetization that give rise to high-frequency magnetic noise. High-frequency magnetic noise is an intrinsic property of magnetic devices in the same way that Johnson noise is a fundamental property of resistors. From the fluctuation-dissipation theorem, high-frequency noise is given by [82]

$$V_n(f) = (I\Delta R)\left[\frac{k_\mathrm{B}T}{2\pi\mu_0 M_\mathrm{s}^2 V f}\chi_\mathrm{t}''(f)\right]^{0.5}, \tag{10}$$

where f is the frequency, I is the device current, ΔR is the change in resistance between parallel and antiparallel states, T is the device temperature, V is the device volume, and χ_t'' is the imaginary part of transverse susceptibility. This equation predicts that noise power is proportional to the imaginary part of transverse susceptibility and inversely proportional to device volume. As device sizes continue to shrink and operating frequencies continue to increase, high-frequency magnetic noise may pose a fundamental limitation to device performance [81,82]. Regardless of the practical implications of high frequency magnetic noise, it is clear that noise spectroscopy is a powerful technique for determining the high-frequency characteristics of magnetic nanostructures. The smaller the structure, the better the technique becomes.

To a first approximation, we can consider the transverse susceptibility in (10) as uniform-mode susceptibility. However, thermal noise will excite all of the magnetization modes, and susceptibility can, more generally, be interpreted as a weighted sum across different modes.

Some noise characteristics of a 1 μm × 3 μm spin valve are shown in Fig. 39. These data were taken by measuring the noise spectra with a spectrum analyzer and subtracting it from a reference spectra in which the device magnetization was saturated along the hard axis. This magnetic noise is, therefore, the noise component due to magnetic fluctuations; other noise components have been subtracted. The top plot shows the voltage noise for different longitudinal bias fields and is similar to susceptibility curves shown in Fig. 24. The FMR resonance is clearly seen and shifts as expected with longitudinal bias field. The lower plot shows the noise spectra at several temperatures between 100 and 400 K. The changes in noise spectra with temperature are due to changing magnetostatic anisotropy, which is proportional to $M_\mathrm{s}(T)$, other temperature-dependent anisotropic energies, and the $k_\mathrm{B}T$ prefactor in (10).

Figure 40 shows a fit to noise data using (10). Here, H_k, α, and an overall scale factor are allowed to vary. The fit is reasonably good. There are some differences between the noise data and the measured device susceptibility (susceptibility measurements were discussed in Sect. 4). The measured damping constant is $\alpha = 0.009$, which is smaller than that measured in the

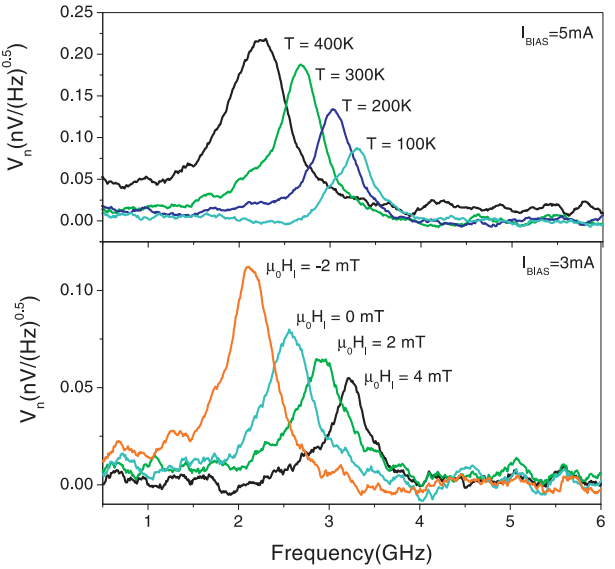

Fig. 39. Magnetic noise of a 1 μm × 3 μm spin valve at various temperatures and in various longitudinal bias fields. The noise voltage shows the FMR peak, which shifts to higher frequencies as the temperature decreases, due to an increase in M_s and associated magnetostatic anisotropies. The data is from [86]

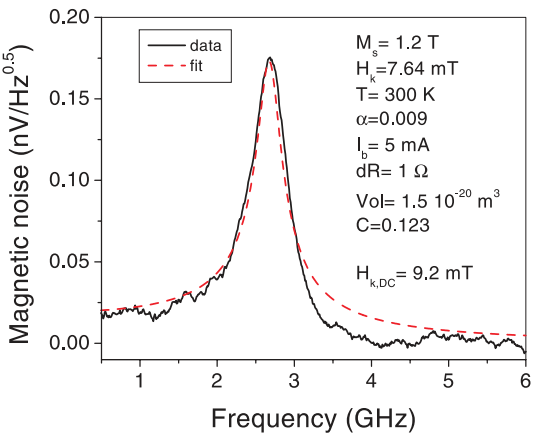

Fig. 40. Fit to magnetic noise of a 1 μm × 3 μm spin valve using (10). For the fit, H_k, α, and C (which is an overall scale factor) were allowed to vary

pulse- and CW-driven rotation experiments. The noise measures small angle fluctuations[15] that are of the order of 0.1 to 0.3°, which is considerably smaller than the 20° rotation measured in Fig. 24. The measured difference in the damping constant may be due to dependence of the damping constant on the size of the magnetization excursion.

A thermal noise field is included in the dynamic models and can also be used to fit the measured response. In dynamic models, the frequency spectrum of the thermal noise field is approximately flat, and the frequency dependence comes predominantly from the dynamic equations (and thereby the proportionality to the device susceptibility). The insets in Fig. 42 show the characteristic fluctuations that are caused in a 0.3 μm × 0.2 μm spin valve by the thermal field. When damping is low, there are strong fluctuations near the resonance frequency. When damping is large, the fluctuations have a frequency spectrum that is relatively flat up to the resonance frequency.

Thermally activated processes, such as those that give rise to $1/f$ and high-frequency magnetic noise, can play a crucial role in switching a magnetic device if the device is switched slowly. For slow quasi-static switching, the device follows a minimum energy trajectory (this corresponds to propagation along the bottom of a complex energy surface such as that shown in Fig. 28). Fluctuations can change the local configuration of the energy surface or allow the system to be thermally activated over energy barriers. These thermally activated processes appear up as time-dependence of a switching event in a critical field region. This is shown in Fig. 41, which depicts the response of a spin-valve device to a field pulse with a value just below the zero-temperature switching field. The switching event is initiated by thermal

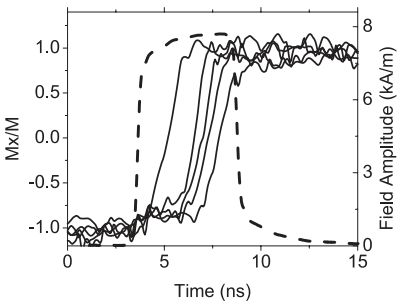

Fig. 41. Switching of a 0.9 μm × 4.2 μm spin valve driven by a 10.9-mT reversal field *(dotted line)*. Time-resolved output signals for several switches are shown *(solid lines)*. The variable dwell time before switching occurs is an indication of thermal activation over a barrier

[15] The rms magnetization variation is given by $\frac{M_{\mathrm{rms}}}{M_{\mathrm{s}}} = \left(\frac{k_{\mathrm{B}}T}{\mu_0 M_{\mathrm{s}} H_{\mathrm{k}} V}\right)^{0.5}$, or it can be obtained by integrating the noise power spectrum [83]

fluctuation, and therefore there is a distribution of switching times. Depending on the type and energy of the thermal fluctuation required to initiate the switching process, the switching time may range from nanoseconds, to seconds, to years. There has been a considerable amount of work on thermal activation processes in the critical field region [73,74]. These studies can give insight into the details and defect structure of a magnetic device. However, from an applications perspective, it is better to operate in the dynamic regime where the device energy remains well above the disordered energy surface. A simple analogy is that it is a more predictable and controllable journey to fly over mountains than to walk over them.

7 Engineering High-Frequency Dynamic Properties

After the high-frequency performance of magnetic devices is measured and characterized, the next step is to control and engineer the high-frequency properties. The two main parameters that control high-frequency performance are the stiffness fields (the sum of anisotropic and applied fields) and the magnetic damping constant. The stiffness fields, which determine the low-frequency susceptibility and the resonance frequency, can be controlled by adjusting the geometry of the device (film thickness and device shape) and by applying bias fields, as is done for abutting permanent magnets. Engineering the damping constant, which controls the height and width of the resonant peak, has only recently been addressed.

For frequency-domain microwave applications, such as tuned filters and circulators, it is usually desirable to minimize damping. For real-time applications, such as high-speed read sensors and MRAM elements, it may be more desirable to have the magnetic system critically damped. An example in Fig. 42 shows the simulated response of a spin-valve read head to a series of fast (200-ps duration) field pulses. The responses of an underdamped ($\alpha = 0.03$) device and a critically damped($\alpha = 0.12$) device are shown. The precessional ringing causes complicated interference between the responses to successive pulses. Although the peak response is slightly less in the critically damped system, it provides a more faithful representation of the applied field pulses. In this example, the bandwidth of the applied field pulses significantly overlapped the FMR peak of the sensor. One can always avoid ringing by pushing the resonant frequency higher by applying larger stiffening fields. However, this results in signal loss because susceptibility falls off inversely with the stiffness field amplitude.

Another example of improved performance is shown in Fig. 43, which depicts a micromagnetic simulation of the switching characteristics of a critically damped MRAM element. The switching is well behaved and has no long-lived oscillations or magnetic noise as is seen in an underdamped switch, such as that shown in Fig. 38.

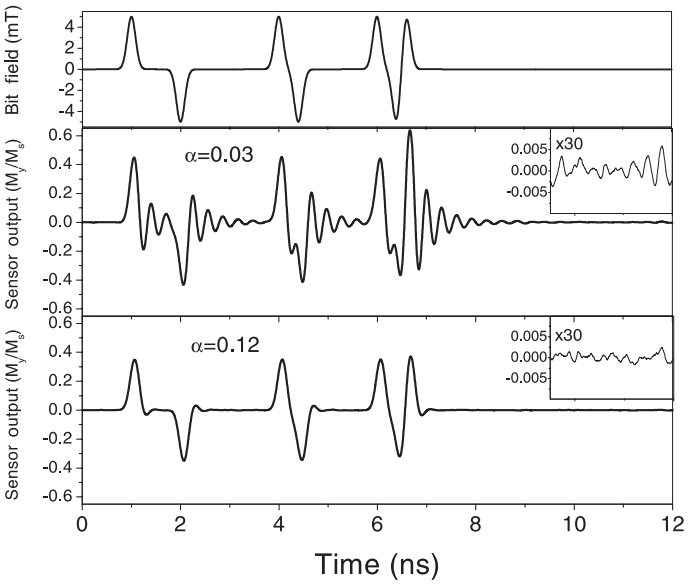

Fig. 42. Single-domain simulation of a 0.3 μm × 0.2 μm spin valve ($H_1 = 5.0$ mT, $T = 350$ K) responding to simulated fields from a bit sequence. The *upper frame* shows the magnetic field profiles; the *middle frame* shows the response of an underdamped spin valve with $\alpha = 0.03$; the *third frame* shows the response of a critically damped spin valve with $\alpha = 0.12$. The *insets* are magnified views of the device magnetization in the quiescent state, which show thermal magnetization fluctuations. The underdamped spin valve shows large fluctuations near the resonance frequency; the critically damped device shows fluctuations that have a flatter frequency spectrum

Magnetic damping can be increased in a number of ways. One way is doping with rare-earth elements that have large orbital moments. The spins in the transition metal couple to the orbital moment (and the associated anisotropic electron density) of the dopant atoms. When the transition-metal spin moment rotates, there are local distortions in the lattice around the rare-earth impurity sites that efficiently couple the magnetic energy into the lattice (phonons). An example of increased damping is shown in Fig. 44, which depicts pulsed inductive measurements [38] of a $Ni_{0.8}Fe_{0.2}$ film and a 2% Tb-doped $Ni_{0.8}Fe_{0.2}$ film. The $Ni_{0.8}Fe_{0.2}$ is underdamped with a damping constant of $\alpha = 0.0082$, and the 2% Tb-doped film is close to critical damping (the point at which oscillations disappear) with a damping constant of $\alpha = 0.0124$. Figure 45a shows the dependence of the damping constant (as measured by pulsed inductive techniques and FMR) as a function of the Tb-doping concentration. Also shown is the damping constant for Gd-doped $Ni_{0.8}Fe_{0.2}$ films, which show little increase in the damping constant as expected because Gd is an *S*-state ion.

Increasing magnetic damping is straightforward, but the critical issue is whether magnetic damping can be engineered while preserving the other

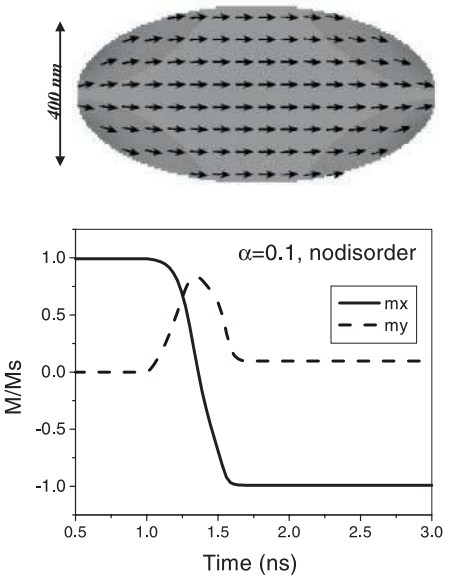

Fig. 43. OOMMF simulation of switching in a critically damped MRAM device (20.0-mT, 200-ps longitudinal pulse; $H_t = 3.0\,\mathrm{mT}$; $\alpha = 0.1$)

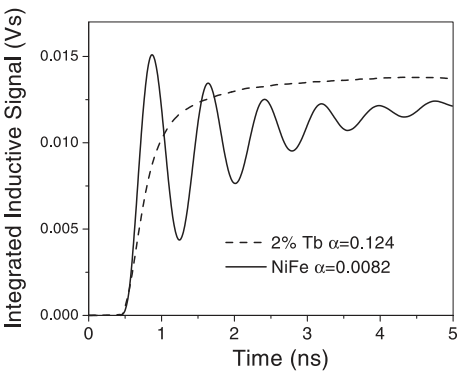

Fig. 44. Time dependence of the integrated inductive voltage of undoped $Ni_{0.8}Fe_{0.2}$ film and a 2% Tb-doped $Ni_{0.8}Fe_{0.2}$ film driven by a fast rise-time (50-ps) transverse step pulse. The integrated voltage signal is proportional to the transverse magnetization [38]

desirable properties of magnetic films. In general, the coercivity, easy-axis anisotropy energy, and magnetostriction are increased by rare-earth doping. However, because damping increases very fast with rare-earth doping, only a small concentration is required for critical damping (1–2%), and most of the desired properties can be maintained [84,85]. This is shown in Fig. 45b, which depicts the dependence of magnetostriction on rare-earth doping. Magnetostriction can be maintained in a reasonable range, even when the system is critically damped.

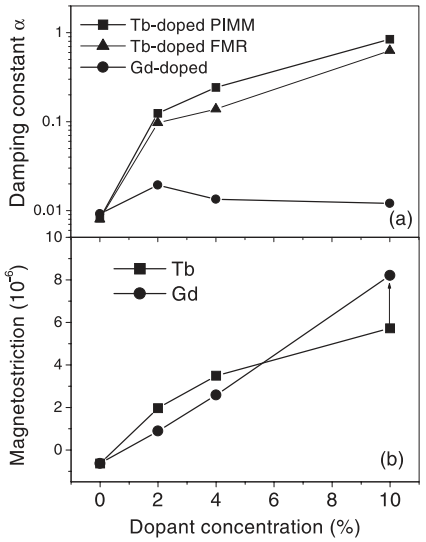

Fig. 45. (**a**) Dependence of the damping constant of $Ni_{0.8}Fe_{0.2}$ films on Tb and Gd doping. (**b**) Dependence of the magnetostriction of $Ni_{0.8}Fe_{0.2}$ films on Tb and Gd doping

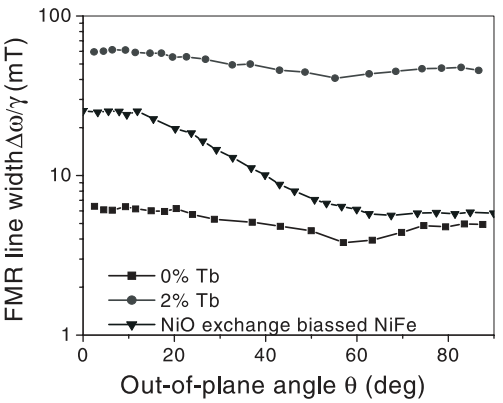

Fig. 46. Dependence of FMR frequency line width on the out-of-plane magnetization angle for $Ni_{0.8}Fe_{0.2}$, $Ni_{0.8}Fe_{0.2}$ on NiO, and 2% Tb-doped $Ni_{0.8}Fe_{0.2}$ films

One of the key issues in engineering damping is the nature of the energy flow path. If the magnetic energy in long-wavelength excitations is transferred to short-wavelength spin waves and not directly to the lattice, then the device's performance may not be improved. The excess energy in a magnetic system will lead to magnetic fluctuations or noise after magnetization rotation or switching has taken place. This can be seen in Fig. 38. These fluctuations can dramatically affect the reversal properties of small magnetic elements. Hence, energy flow from long-wavelength magnetization motion into short wavelength spin waves does not constitute a relaxation process. One must wait until the energy is removed from the entire magnetic system if one needs consistent, reproducible device response. One method of characterizing the type of relaxation processes present is measuring the angular dependence of the FMR line width. Disorder-mediated coupling to spin waves

(two-magnon processes) shows dependence on the spin-wave density of states. In general, there is a higher density of degenerate spin waves when magnetization lies in the plane of the film. As magnetization is rotated out of the film plane, the number of degenerate spin waves decreases and hence the damping (or FMR line width) should decrease. Figure 46 shows the angle-dependent FMR line width for a series of different $Ni_{0.8}Fe_{0.2}$ films. An exchange-biased $Ni_{0.8}Fe_{0.2}$ film on NiO shows strong angular dependence, indicating that there is strong coupling to spin waves presumably mediated by magnetic disorder at the ferromagnetic–antiferromagnetic interface. Both $Ni_{0.8}Fe_{0.2}$ and Tb-doped $Ni_{0.8}Fe_{0.2}$ films show little angular dependence, suggesting that damping, in these cases, is not dominated by spin-wave relaxation.

Acknowledgments

We thank Pavel Kabos and Tom Silva for their expertise in magnetodynamics and for their assistance in developing high-frequency magnetic measurements. This work was supported in part by the DARPA Spintronics Program and the NIST Nanomagnetodynamics Program.

References

1. D. O. Smith: Magnetization reversal and thin films, J. Appl. Phys. **29**, 264 (1958) 93
2. C. D. Olson, A. V. Pohm: Flux reversal in thin films of 82% Ni, 18% Fe, J. Appl. Phys. **29**, 274 (1958) 93
3. W. Dietrich, W. E. Proebster, P. Wolf: Nanosecond switching in thin films, IBM J. **189**, 189 (1960) 93
4. A. B. Smith: *Bubble-Domain Memory Devices* (Artech House, Norwood MA 1974) 94
5. T. H. O'Dell: *Magnetic Bubbles* (Wiley, New York 1974) 94
6. M. R. Freeman, W. K. Hiebert: Stroboscopic microscopy of magnetic dynamics, in B. Hillebrands, K. Ounadjela (Eds.): *Spin Dynamics in Confined Magnetic Structures I*, (Topics Appl. Phys. **83**) (Springer, Berlin, Heidelberg 2002) 94
7. D. A. Thompson, L. T. Romankiw, A. F. Mayadas: Thin film magnetoresistors in memory, storage, and related applications, IEEE Trans. Magn. **11**, 1039 (1975) 94
8. A. V. Pohm, J. S. T. Huang, J. M. Daughton, D. R. Krahn, V. Mehra: The design of a one megabit non-volatile M-R memory chip using $1.5 \times 5\,\mu m$ cells, IEEE Trans. Magn. **24**, 3117 (1988) 94
9. M. N. Baibich, J. M. Broto, A. Fert, F. Nguyen Van Dau, F. Petroff, P. Eitenne, G. Creuzet, A. Friederich, J. Chazelas: Giant magnetoresistance of (001)Fe/(001)Cr magnetic superlattices, Phys. Rev. Lett. **61**, 2472–2475 (1988) 94, 95
10. G. Binasch, P. Grunberg, F. Saurenbach, W. Zinn: Enhanced magnetoresistance in layered magnetic structures with antiferromagnetic interlayer exchange, Phys. Rev. B **39**, 4828 (1989) 94

11. J. S. Moodera, L. R. Kinder, T. M. Wong, R. Meservey: Large magnetoresistance at room temperature in ferromagnetic thin film tunnel junctions, Phys. Rev. Lett. **74**, 3273 (1995) 94
12. R. Schad, P. Belien, G. Verbanck, C. D. Potter, H. Fischer, S. Lefebvre, M. Bessiere, V. V. Moshchalkov, Y. Bruynseraede: Quantitative study of the interdependence of interface structure and giant magnetoresistance in polycrystalline Fe/Cr superlattices, Phys. Rev. B **57**, 13692 (1998) 95
13. S. S. P. Parkin, Z. G. Li, D. J. Smith: Giant magnetoresistance in antiferromagnetic Co/Cu multilayers, Appl. Phys. Lett. **58**, 2710 (1991) 95
14. A. P. Ramirez: Colossal magnetoresistance, J. Phys. Condens. Matter **9**, 8171 (1997) 95
15. R. E. Camley, J. Barnas: Theory of giant magnetoresistance effects in magnetic layered structures with antiferromagnetic coupling, Phys. Rev. Lett. **63**, 664 (1989) 95
16. P. LeClair, J. T. Kohlhepp, C. H. van de Vin, H. Wieldraaijer, H. J. M. Swagten, W. J. M. de Jonge, A. H. Davis, J. M. MacLaren, J. S. Moodera, R. Jansen: Band structure and density of states effects in Co-based magnetic tunnel junctions, Phys. Rev. Lett. **88**, 107201 (2002) 95
17. W. H. Butler, X.-G. Zhang, T. C. Schulthess, D. M. C. Nicholson, A. B. Oparin, J. M. MacLaren: First principles modeling of magnetic random access memory devices, J. Appl. Phys. **85**, 5834 (1999) 95
18. W. H. Butler, O. Heinonen, X. G. Zhang: Theory of magnetotransport for magnetic recording, in *The Physics of Ultra High Density Recording*, M. L. Plumer, J. Vank, D. Weller (Eds.) (Springer, Berlin, Heidelberg 2001) p. 277 95
19. A. Vedyayev, N. Ryzhanova, B. Dieny, P. Dauguet, P. Gandit, J. Chaussy: Angular variation of giant magnetoresistance for current perpendicular to the plane of the layers, Phys. Rev. B **55**, 3728 (1997) 96
20. B. Dieny, V. S. Speriosu, S. S. P. Parkin, B. A. Gurney, D. R. Wilhoit, D. Mauri: Giant magnetoresistance in soft ferromagnetic multilayers, Phys. Rev. B **43**, 1297 (1991) 96, 97
21. J. L. Leal, M. H. Kryder: Spin valves exchange biased by Co/Ru/Co synthetic antiferromagnets, J. Appl. Phys. **83**, 3720 (1998) 97
22. A. E. Berkowitz, K. Takano: Exchange anisotropy – a review, J. Magn. Magn. Mater. **200**, 552 (1999) 98
23. D. D. Tang, P. K. Wang, V. S. Speriosu, S. Le, K. K. Kung: Spin-valve RAM cell, IEEE Trans. Magn. **31**, 3206 (1995) 98
24. B. A. Everitt, A. V. Pohm, J. M. Daughton: Size dependence of switching thresholds for pseudospin valve MRAM cells, J. Appl. Phys. **81**, 4020 (1997) 99
25. S. S. P. Parkin, K. P. Roche, M. G. Samant, P. M. Rice, R. B. Beyers, R. E. Scheuerlein, E. J. O'Sullivan, S. L. Brown, J. Bucchigano, D. W. Abraham, Yu Lu, M. Rooks, P. L. Trouilloud, R. A. Wanner, W. J. Gallagher: Exchange-biased magnetic tunnel junctions and application to nonvolatile magnetic random access memory, J. Appl. Phys. **85**, 5828 (1999) 100
26. W. F. Egelhoff, Jr., P. J. Chen, C. J. Powell, M. D. Stiles, R. D. McMichael, J. H. Judy, K. Takano, A. E. Berkowitz: Oxygen as a surfactant in the growth of giant magnetoresistance spin valves, J. Appl. Phys. **82**, 6142 (1997) 100
27. L. Neel: On a new mode of coupling between the magnetizations of two ferromagnetic layers, Compte. Rend. Acad. Sci. France **255**, 1676 (1962) 100

28. A. Aharoni: Demagnetizing factors for rectangular ferromagnetic prisms, J. Appl. Phys **83**, 3432 (1998) 103
29. A. J. Newell, W. Williams, D. J. Dunlop: A generalization of the demagnetizing tensor for nonuniform magnetization, J. Geophys. Res. **98**, 9551 (1993) 103
30. R. W. Cross, Young K. Kim, J. O. Oti, S. E. Russek: Magnetostatic effects in giant magnetoresistive spin-valve devices, Appl. Phys. Lett. **69**, 3935 (1996) 104
31. W. F. Brown: Thermal fluctuations of a single-domain particle, Phys. Rev. **130**, 1677 (1963) 104
32. C. E. Patton: Linewidth and relaxation processes for the main resonance in the spin-wave spectra of Ni-Fe films, J. Appl. Phys. **39**, 3060 (1968) 102, 105
33. J. van Elk, M. Plummer: Introduction to micromagnetic recording physics, in M. L. Plumer, J. Van Ek, D. Weller (Eds.) *The Physics of Ultra High Density Recording* (Springer, Berlin, Heidelberg 2001) p. 1 101
34. V. L. Safonov, H. N. Bertram: Magnetization dynamics and thermal fluctuations in fine grains and thin films, in M. L. Plumer, J. Van Ek, D. Weller (Eds.) *The Physics of Ultra High Density Recording* (Springer, Berlin, Heidelberg 2001) p. 81 101
35. T. J. Silva: Measurement of dynamic properties in thin films, in M. L. Plumer, J. Van Ek, D. Weller (Eds.) *The Physics of Ultra High Density Recording* (Springer, Berlin, Heidelberg 2001) p. 110 101
36. J. Miltat, G. Albuquerque, A. Thiaville: An introduction to micromagnetics in the dynamical regime, in B. Hillebrands, K. Ounadjela (Eds.) *Spin Dynamics in Confined Magnetic Structures I*, Topics Appl. Phys. **83** (Springer, Berlin, Heidelberg 2002) 101, 110, 112
37. R. D. McMichael, M. D. Stiles, P. J. Chen, W. F. Egelhoff, Jr.: Ferromagnetic resonance line width in thin films coupled to NiO, J. Appl. Phys. **83**, 7037 (1998) 102
38. T. J. Silva, C. S. Lee, T. M. Crawford, C. T. Rogers: Inductive measurement of ultrafast magnetization dynamics in thin-film permalloy, J. Appl. Phys. **85**, 7849 (1999) 102, 105, 147, 148
39. E. C. Stoner, E. P. Wohlfarth: A mechanism of magnetic hysteresis in heterogeneous alloys, Philos. Trans. R. Soc. London **A240**, 599 (1948). Reprinted in IEEE Trans. Magn. **27**, 3475 (1991) 105, 125
40. R. D. McMichael, M. J. Donahue, D. G. Porter, J. Eicke: Comparison of magnetostatic field calculation methods on 2-D square grids as applied to a micromagnetic standard problem, J. Appl. Phys. **85**, 5816 (1999) 111
41. M. J. Donahue, D. G. Porter, R. D. McMichael, J. Eicke: Behavior of muMAG standard problem No. 2 in the small particle limit, J. Appl. Phys. **87**, 5520 (2000) 111
42. R. D. McMichael, M. J. Donahue, D. G. Porter, J. Eicke: Switching dynamics and critical behavior of standard problem No. 4, J. Appl. Phys. **89**, 7603 (2001) 111
43. M. J. Donahue, R. D. McMichael: Exchange energy representations in computational micromagnetics, Physica B **233**, 272 (1997) 111
44. M. J. Donahue, D. G. Porter: OOMMF User's Guide, Version 1.0, Interagency Report NISTIR 6376 (National Institute of Standards and Technology, Gaithersburg, MD 1999) 111
45. D. G. Porter: Analytical determination of the LLG zero-damping critical switching field, IEEE Trans. Magn. **34**, 1663 (1998)

46. O. Gérardin, H. Le Gall, M. J. Donahue, N. Vukadinovic: Micromagnetic calculation of the high frequency dynamics of nano-size rectangular ferromagnetic stripes, J. Appl. Phys. **89**, 7012 (2001) 115
47. J. Gadbois, J. Zhu, W. Vavra, A. Hurst: The effect of end and edge shape on the performance of pseudo-spin valve memories, IEEE Trans. Magn. **34**, 1066 (1998) 115
48. R. H. Koch, J. G. Deak, D. W. Abraham, P. L. Trouilloud, R. A. Altman, Yu Lu, W. J. Gallagher, R. E. Scheuerlein, K. P. Roche, S. S. P. Parkin: Magnetization reversal in micron-sized magnetic thin films, Phys. Rev. Lett. **81**, 4512 (1998) 115, 125
49. J. Deak, R. H. Koch: The effect of edge roughness on magnetization reversal in micron-sized permalloy thin films, J. Magn. Magn. Mater. **213**, 25 (2000) 115
50. J.-G. Zhu, Y. Zheng: The micromagnetics of random access memory, in B. Hillebrands, K. Ounadjela (Eds.) *Spin Dynamics in Confined Magnetic Structures I*, Topics Appl. Phys. **83** (Springer, Berlin, Heidelberg 2002) 115
51. R. D. McMichael, M. J. Donahue: Head to head domain wall structures in thin magnetic strips, IEEE Trans. Magn. **33**, 4167 (1997) 118
52. R. P. Cowburn, D. A. Allwood, G. Xiong, M. D. Cooke: Domain wall injection and propagation in planar Permalloy nanowires, J. Appl. Phys. **91**, 6949 (2002) 118
53. R. D. McMichael, J. Eicke, M. J. Donahue, D. G. Porter: Domain wall traps for low-field switching of sub-micron elements, J. Appl. Phys. **87**, 7058 (2000) 118
54. P. Kabos, S. Kaka, S. E. Russek, T. J. Silva: Metastable states in large angle magnetization rotations, IEEE Trans. Magn. **36**, 3050 (2000)
55. S. E. Russek, S. Kaka, M. J. Donahue: High-speed dynamics, damping, and relaxation times in submicrometer spinvalve devices, J. Appl. Phys. **87**, 7070 (2000) 125
56. J. O. Oti, S. E. Russek: Micromagnetic simulations of magnetoresistive behavior of sub-micrometer spin valve MRAM devices, IEEE Trans. Magn. **33**, 3298 (1997)
57. R. W. Cross, J. O. Oti, S. E. Russek, T. Silva, Y. K. Kim: Magnetoresistance of thin-film NiFe devices exhibiting single-domain behavior, IEEE Trans. Magn. **31**, 3358 (1995)
58. J. O. Oti, R. W. Cross, S. E. Russek, Y. K. Kim: Simulating device size effects on magnetization pinning mechanisms, J. Appl. Phys. **79**, 6386 (1996)
59. S. E. Russek, J. O. Oti, Y. K. Kim, R. W. Cross: Field angle and current density effects in submicrometer spin valves for digital applications, IEEE Trans. Magn. **33**, 3292 (1997)
60. S. E. Russek, J. O. Oti, Y. K. Kim: Switching characteristics of spin valve devices designed for MRAM applications, J. Magn. Magn. Mater. **199**, 6 (1999) 101, 126
61. J. O. Oti: A micromagnetic model of dual-layer magnetic-recording thin films, IEEE Trans. Magn. **29**, 1265 (1993)
62. J. O. Oti, Y. K. Kim, S. Suvarna: A personal computer based semi-analytical micromagnetics design tool, IEEE Trans. Magn. **33**, 4119 (1997)
63. H. Javadi: Microwave Materials, in *Handbook of Microwave Technology*, Vol. 2, T. Ishii (Ed.), (Academic Press, San Diego 1995) pp. 605–643 122
64. S. E. Russek, J. O. Oti, S. Kaka, E. Y. Chen: High-speed characterization of submicrometer giant magnetoresistive devices, J. Appl. Phys. **85**, 4773 (1999) 125

65. S. Kaka, S. E. Russek: Switching in spin-valve devices in response to subnanosecond longitudinal field pulses, J. Appl. Phys. **87**, 6391 (2000) 125, 136
66. S. E. Russek, S. Kaka: Time and frequency domain measurements of ferromagnetic resonance in small spin-valves, IEEE Trans. Magn. **36**, 2560 (2000) 126, 128
67. H. W. Schumacher, C. Chappert, P. Crozat, R. C. Sousa, P. P. Freitas: Coherently suppressed ringing of the magnetization in microscopic giant magnetoresistive devices, J. Appl. Phys. **91**, 8043 (2002) 125
68. H. W. Schumacher, C. Chappert, P. Crozat, R. C. Sousa, P. P. Freitas, M. Bauer: Coherent suppression of magnetic ringing in microscopic spin valve elements, Appl. Phys. Lett. **80**, 3781 (2002) 125
69. S. Tehrani, B. Engel, J. Slaughter, E. Y. Chen, M. DeHerrera, M. Durlam, P. Naji, R. Whig, J. Janesky, J. Calder: Recent developments in magnetic tunnel junction MRAM, IEEE Trans. Magn. **36**, 2752 (2000) 125, 130
70. W. H. Rippard, A. C. Perrella, P. Chalsani, F. J. Albert, J. A. Katine, R. A. Buhrman: Observation of magnetization reversal of thin-film permalloy nanostructures using ballistic electron magnetic microscopy, Appl. Phys. Lett. **77**, 1357 (2000) 130
71. J. Shi, S. Tehrani, M. R. Scheinfein: Geometry dependence of magnetization vortices in patterned submicron NiFe elements, Appl. Phys. Lett. **76**, 2588 (2000) 130
72. A. Anguelouch, B. D. Schrag, Gang Xiao, Yu Lu, P. L. Trouilloud, R. A. Wanner, W. J. Gallagher, S. S. P. Parkin: Two-dimensional magnetic switching of micron-size films in magnetic tunnel junctions, Appl. Phys. Lett. **76**, 622 (2000) 130
73. R. H. Koch, G. Grinstein, G. A. Keefe, Yu Lu, P. L. Trouilloud, W. J. Gallagher, S. S. P. Parkin: Thermally assisted magnetization reversal in submicron-sized magnetic thin films, Phys. Rev. Lett. **84**, 5419 (2000) 134, 146
74. N. D. Rizzo, M. DeHerrera, J. Janesky, B. Engel, J. Slaughter, S. Tehrani: Thermally activated magnetization reversal in submicron magnetic tunnel junctions for magnetoresistive random access memory, Appl. Phys. Lett. **80**, 2335 (2002) 134, 146
75. S. Kaka, S. E. Russek: Precessional switching of submicrometer spin valves, Appl. Phys. Lett. **80**, 2958 (2002) 138
76. T. Gerrits, H. A. M. van den Berg, J. Hohlfeld, L. Bar, T. Rasing: Ultrafast precessional magnetization reversal by picosecond magnetic field pulse shaping, Nature **418**, 509 (2002) 138
77. H. T. Hardner, S. S. P. Parkin, M. B. Weissman, M. B. Salamon, E. Kita: $1/f$ noise in giant magnetoresistive materials, J. Appl. Phys. **75**, 6531 (1994) 142
78. L. S. Kirschenbaum, C. T. Rogers, S. E. Russek, S. C. Sanders: Telegraph noise in silver-Permalloy giant magnetoresistance test structures, IEEE Trans. Magn. **31**, 3943 (1995) 142
79. L. S. Kirschenbaum, C. T. Rogers, S. E. Russek, Y. K. Kim: Low-frequency noise in NiFe/Cu spin-valves, IEEE Trans. Magn. **33**, 3586 (1997) 142
80. S. Ingvarsson, Gang Xiao, R. A. Wanner, P. Trouilloud, Yu Lu, W. J. Gallagher, A. Marley, K. P. Roche, S. S. P. Parkin: Electronic noise in magnetic tunnel junctions, J. Appl. Phys. **85**, 5270 (1999) 142
81. N. Smith, P. Arnett: White-noise magnetization fluctuations in magnetoresistive heads, Appl. Phys. Lett. **78**, 1448 (2001) 143

82. N. Smith: Modeling of thermal magnetization fluctuations in thin-film magnetic devices, J. Appl. Phys. **90**, 5768 (2001) 143
83. L. D. Landau, E. M. Liftshitz: *Statistical Physics* (Pergamon, New York 1980) Chap. 12 145
84. W. E. Bailey, P. Kabos, F. Mancoff, S.E. Russek: Control of magnetization dynamics in $Ni_{81}Fe_{19}$ thin films through the use of rare-earth dopants, IEEE Trans. Magn. **37**, 1749 (2001) 148
85. S. E. Russek, P. Kabos, R. D. McMichael, C. G. Lee, W. E. Bailey, R. Ewasko, S. C. Sanders: Magnetostriction and angular dependence of ferromagnetic resonance linewidth in Tb-doped $Ni_{0.8}Fe_{0.2}$ thin films, J. Appl. Phys. **91**, 8659 (2002) 148
86. N. Stuzke, S. L. Burkett, S. E. Russek: Temperature and field dependence of high-frequency magnetic noise in spin valve devices, Appl. Phys. Lett. **82**, 91 (2003) 144

Index